UNIVERSITÀ DEGLI STUDI DI PADOVA

Dipartimento di Fisica e Astronomia "Galileo Galilei"

Master Degree in Physics

Final Dissertation

Radiation Asymmetry during disruptions in JET device

Oxford, United Kingdom

Thesis supervisor

Prof Lidia Piron

Thesis co-supervisor

Dr. Mengdi Kong

Candidate

Tancredi Lo Presti Piccolo

Academic Year 2022/2023

Abstract

The plasma stored energy in a burning plasma pulse, as in ITER, will significantly exceed that in present tokamaks. The rapid release of this energy during a plasma disruption, which is a dramatic event during which confinement is suddenly destroyed [TokW], has the potential to cause melting of the first wall and cause high electromagnetic loads close to the design limits. It is thus of crucial importance establish reliable and effective strategies to avoid and, as a final line of defence, to mitigate disruptions.

In this Thesis project, a mitigation technique named the Shattered Pellet Injection system (SPI), has been investigated considering experiments carried out at the JET device, located at Culham Centre for Fusion Energy (CCFE, Oxfordshire, UK). JET is a suitable machine to perform this study being equipped with a Beryllium and Tungsten as wall materials, as in ITER.

The mitigation via SPI relies on fast impurity injection in the form of frozen pellets, usually Deuterium and Argon or Neon, which allow the plasma energy to be released as radiation. SPI is the disruption mitigation system adopted in ITER and to provide an effective SPI action, without damaging first-wall components, the radiation shall be spread toroidally [Jachmich22].

This project has focused on understanding the mitigation dynamics via SPI and calculating from experimental data and a 1D radiation model the toroidal peaking factor, a metrics that describes the level of radiation asymmetry.

This work followed the studies reported in [Lehnen15],[Jachmich22] and considered a database of Ohmic and H-mode experiments where the SPI has been fired. The distribution of radiation has been inferred from the change of the radiated power measured at a given toroidal location as a function of the location of the phase of the locked mode [TokW]. The location of the locked mode has been tailored by using the Error field correction coils.

A workflow has been established, which includes data analysis from multiple diagnostics and 1D modelling implemented in the Python framework [GitHub].

The main findings obtained in this project are: the radiation asymmetry content is maximal when the mode locking occurs close to the injection location, and plasmas with higher thermal content, such as H-mode plasmas, result in lower asymmetries hence more manageable load, which is consistent with previous results ([Lehnen15],[Jachmich22]).

Contents

Chapter 1

Physics of Magnetically Confined Fusion Plasmas

In this chapter, the physics of thermonuclear fusion plasmas is briefly presented, explaining its origins and the confinement methods. The tokamak device is also introduced, together with the most important machine protection method: the shattered pellet injector, and the radiation asymmetry study, which is the main topic of this Thesis project.

1.1 Fusion Technology

Thermonuclear fusion represents a clean, sustainable and reliable source of energy, which has motivated researchers on plasma physics for several decades. Moreover, in contrast to fission and fossil fuels, it has the advantage of not producing either long-lasting radioactive waste and greenhouse effects.

1.1.1 Thermonuclear fusion reactor in a nutshell

Thermonuclear fusion is referred as the nuclear reaction among two light nuclei that fuse into a heavier nucleus, releasing energy and other reaction products in the process. Fusion is the basic process through which all stars produce their energy and are able to maintain equilibrium.

Since the 1960s, efforts have been dedicated to reproduce fusion reactions on planet Earth. The reactions between the isotopes of Hydrogen, Deuterium (D) and Tritium (T), are considered as the favourite candidates for technology exploitation of thermonuclear fusion. In particular the main fusion reaction are:

$$\begin{aligned} {}^{2}\mathrm{D} + {}^{2}\mathrm{D} &\longrightarrow {}^{3}\mathrm{He} + \mathrm{n} + 3.27\,\mathrm{MeV} \\ {}^{2}\mathrm{D} + {}^{2}\mathrm{D} &\longrightarrow {}^{3}\mathrm{T} + {}^{1}\mathrm{H} + 4.03\,\mathrm{MeV} \\ {}^{2}\mathrm{D} + {}^{3}\mathrm{T} &\longrightarrow {}^{4}\mathrm{He} + \mathrm{n} + 17.6\,\mathrm{MeV} \\ {}^{2}\mathrm{D} + {}^{3}\mathrm{He} &\longrightarrow {}^{4}\mathrm{He} + {}^{1}\mathrm{H} + 18.4\,\mathrm{MeV} \end{aligned} \tag{1.1}$$

The last two reactions give the most energy output, but it is the D-T reaction the most promising one as it has the highest cross-section at the lowest Deuterium energy, as shown in Fig. 1.1. Therefore, for achieving nuclear fusion, a D-T mixture is heated up until the thermal velocities are sufficiently high for fusion reactions to become likely.

Deuterium is largely abundant on earth, as 33mg of D can be found per every kilo of sea water; it is therefore virtually unlimited for our purposes. On the contrary, Tritium cannot be naturally found as it naturally decays with a mean lifetime of 12.3 year. To overcome this problem, Tritium, in a future fusion reactor, will be produced in the reactor itself, exploiting the Lithium-Neutron fission reactions:

$$\begin{aligned} {}^{6}_{3}\mathrm{Li} + \mathrm{n} &\longrightarrow {}^{4}_{2}\mathrm{He} + {}^{3}_{1}\mathrm{T} + 4.8\,\mathrm{MeV} \\ {}^{7}_{3}\mathrm{Li} + \mathrm{n} &\longrightarrow {}^{4}_{2}\mathrm{He} + {}^{3}_{1}\mathrm{T} + \mathrm{n} - 2.5\,\mathrm{MeV} \end{aligned} \tag{1.2}$$

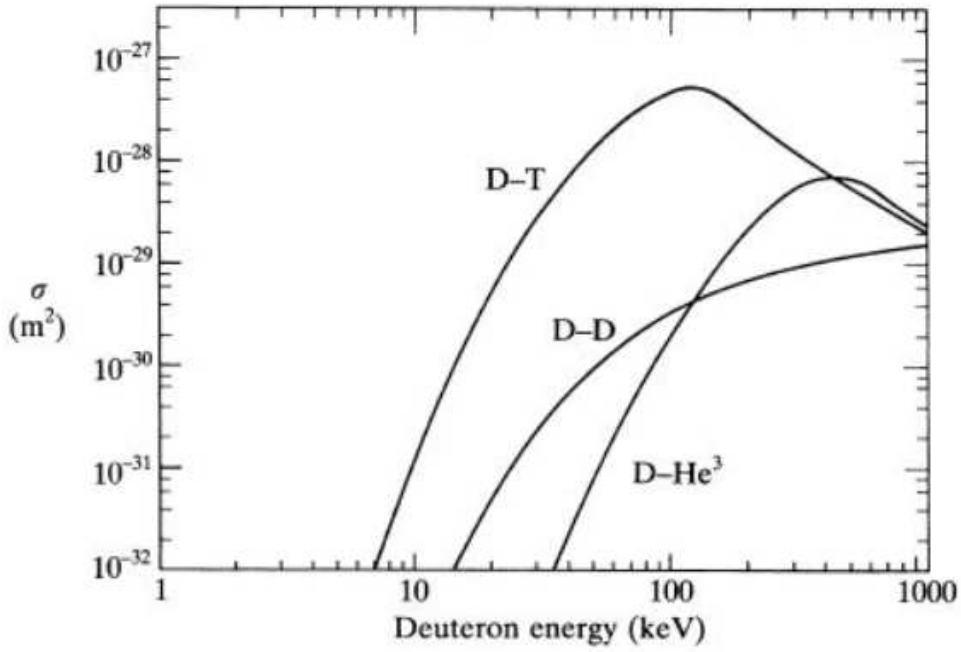

Figure 1.1: Cross-sections of the D-T, D-D, and D-He^3 fusion reactions as a function of Deuteron kinetic energy.

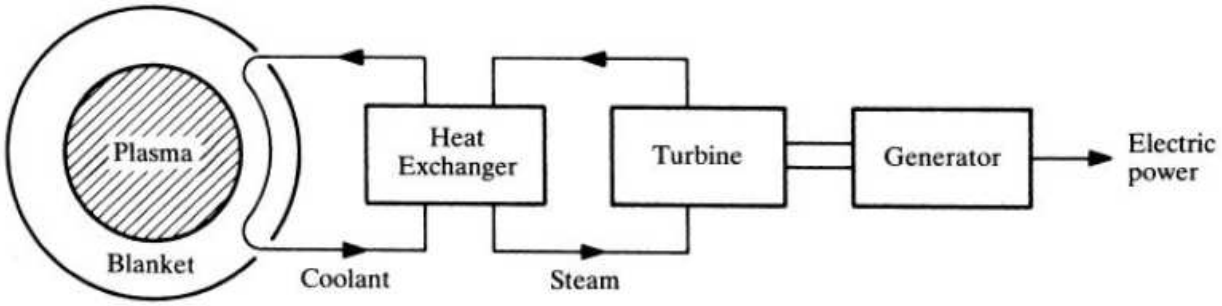

Figure 1.2: Conceptual scheme of a magnetic fusion power plant, showing that energy is collected in the blanket by coolants, transferred to water to turn it into steam and eventually spin turbines for electricity production.

where $_3$Li represents Lithium and n is the symbol for neutrons. This is the working principle of the so-called *breeding blanket* [ITER-blanket]. A conceptual scheme of a magnetic fusion power plant is shown in Fig 1.2.

A major obstacle for a fusion reaction comes from the Coulomb repulsion of charged particles, thus to overcome such barrier particles require very high kinetic energies. Unfortunately, even at enormous energy such 100 keV where the cross-section for the D-T reaction peaks ($\approx$ 1.1 billion Kelvin for temperature reference), the probability of Coulomb scattering is much higher than that of a fusion reaction. To come around this problem, atoms have to be spatially confined in order to have numerous collisions before they undergo a fusion reaction. This can be achieved only in *plasmas*, as temperature are so elevated that Hydrogen (and its isotopes) are completely ionised.

Two different methods to achieve fusion conditions in laboratories have been developed through the years: magnetic confinement and inertial confinement.

- *Magnetic confinement* exploits strong magnetic fields to confine ionised particles in Larmor orbits following magnetic field lines. Macroscopically the plasma gets pinched from the external fields, balancing its pressure and locking it in a confined volume.

- *Inertial confinement* experiments, on the other hand, shine very powerful lasers onto tiny spheres of solid D-T mixtures in order to reach fusion temperatures and densities. The external layers

vaporise, compressing the internal parts and increasing the core density and temperature to fusion levels. Fusion reactions are then confined by the laser-induced shock waves coming from the external layers. This technology will not be covered in this Thesis work.

Let's consider Magnetic fusion devices. In order to produce electricity, the energy balance of a fusion reactor has to be positive, i.e. the energy produced by fusion reactions has to exceed that required to create and sustain the plasma itself. The power balance equation can be written as:

$$\frac{dw}{dt} = p_H + p_\alpha - p_L - p_R \tag{1.3}$$

where $w = 3nT$ is the plasma thermal energy density (in plasma physics k_B is implicit inside T), p_H and p_α are respectively the external heating power and the self-heating power from α-particles, while p_R and p_L represent the power losses from radiation (mainly from bremsstrahlung and impurities) and transport processes.

The total power production from fusion reactions is quantified by the following expression:

$$p_f = \frac{1}{4} n^2 \langle \sigma v \rangle_T E_f \tag{1.4}$$

where $n = n_D = n_T$ is the D-T mixture density, $E_f = 17.6$ MeV is the energy output from a single fusion reaction and finally $\langle \sigma v \rangle_T$ is a quantity called *reactivity*. Deuterium and tritium mixture is a 50-50 density mixture to ensure maximal power output, while reactivity $\langle \sigma v \rangle_T$ is a quantity proportional to the number of occurring reactions per unit volume and time and it is dependent on temperature. For D-T mixes around 10-20 keV, which is the reactor relevant range, reactivity is $\langle \sigma v \rangle_T = 1.1 \times 10^{-24}\ T^2 m^2 s^{-1}$. Finally, in magnetic confinement reactors around 4/5 of the output power escapes the reactor as it is carried by neutrons, which do not interact with the magnetic fields, while the remaining 1/5 goes to α-particle heating.

Focusing instead on the power sinks, as expressed by eq. 1.3 by the negative terms, they are divided in two contributions: radiation and transport losses. In particular, radiation losses can further categorised: Bremsstrahlung and Line radiation losses. The first is due to the numerous collisions between charged particles in the plasma, making them decelerate and accelerate therefore emitting light. Bremsstrahlung is described by the following expression:

$$p_b = \alpha_b n^2 \sqrt{T} \quad W m^{-3} \tag{1.5}$$

where $\alpha_b = 5.35 \times 10^{-37} W m^3 keV^{1/2}$. Line radiation comes from impurities present in the plasma being exited and subsequently relaxing to a lower energy state. Both effects are microscopic mechanisms where each particle contributes individually.

On the contrary transport losses are generalised phenomena; this kind of power sink though is still not theoretically well described, thus to quantify these effect an empirical quantity was introduced, called *energy confinement time* τ_E. The energy confinement time is defined as:

$$P_L = \frac{W}{\tau_E} \tag{1.6}$$

where P_L and W are the power losses and the internal thermal energy, respectively. The idea behind τ_E stems from imaging switching-off of all heating mechanisms of the plasma and then measuring the characteristic exponential energy decay time as the plasma cools off; although this is not how actually τ_E is measured in experiments (nowadays it is calculated from scaling laws), the idea behind the quantity itself is the one mentioned. A better confined plasma will maintain itself hot for a longer time, exactly as a well insulated house will trap the heat inside better than poorly insulated house in cold winter day.

Having introduced the balance Eq. 1.3, it is important to mention the *balancing conditions* of Breakeven and Ignition. A crucial quantity in energy balancing equations is the so-called Q Gain value, basically describing the fusion energy output normalised to the heating energy input in the reactor:

$$Q = \frac{P_f}{P_H} \tag{1.7}$$

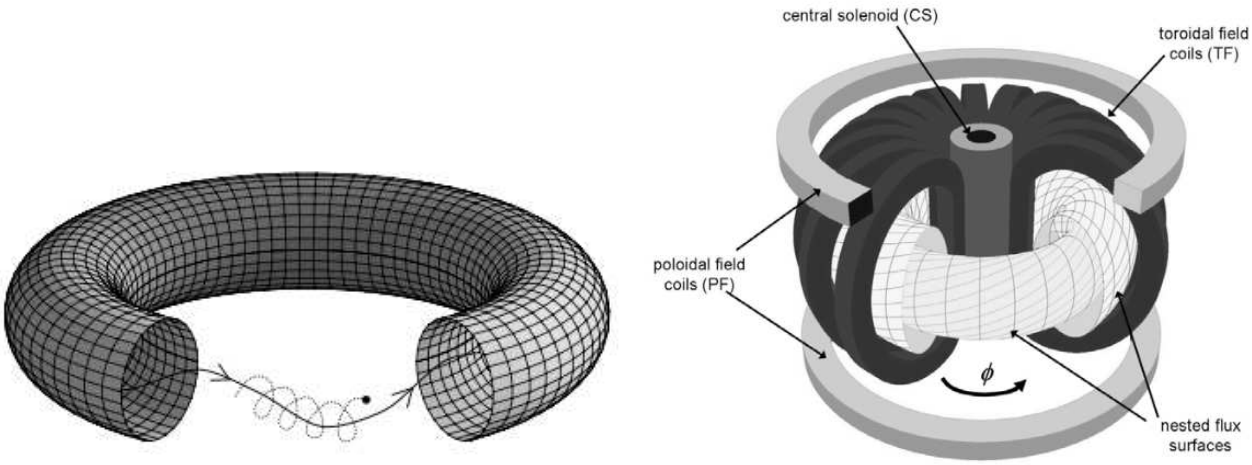

(a) (b)

Figure 1.3: (a) Toroidal geometry. Pictorial magnetic line (solid) and particle trajectory (dashed) is shown as well. (b) Simple sketch of a tokamak.

- *Breakeven*: Q=1. Breakeven condition is achieved when the fusion output matches the energy input required to sustain the reactions going. It is the first imperative step toward a working reactor.
- *Ignition*: Q=∞. This condition describes the situation where no heating is required to sustain fusion reactions, hence $P_H = 0$. The plasma is self-sustaining and no external support is needed. Even though ignition seems the ultimate goal for fusion research, having no external heating means lacking an active control tool essential for many purposes.

Finally the *triple product* is introduced. This quantity is the product between plasma temperature, density and energy confinement time and the mentioned conditions can be rewritten using this quantity. In particular the numerical threshold value depends on the physical characteristics of the process considered (magnetic or inertial), as well as the possible accessible regimes in a given process. Therefore it embodies the performances of the particular experiment or reactor based on the process. For example, the approximated triple product for ignition in a magnetic fusion device in the 10-20 keV range is, assuming flat temperature and density profiles:

$$nT\tau_E \geq 3 \times 10^{21} m^{-3} keV s \tag{1.8}$$

Considering realistic density and temperature profiles an even higher threshold is required.

1.1.2 Tokamaks

In fusion research, several magnetic field geometries have been investigated, such as magnetic mirrors, linear, and toroidal configurations to seek the best conditions for plasma confinement. Among them, the toroidal geometry has given the best confinement performances. This section will be dedicated to a brief introduction to the principles of magnetic plasma confinement in toroidal devices and, in particular, in the so-called *tokamak* configuration.

The name tokamak is a Russian acronym which stands for *toidalnaya kamera* and *magnitnaya katushka*, that is "toroidal chamber" and "magnetic coil". A sketch of a tokamak and toroidal geometry are shown in Fig. 1.3(a) and Fig. 1.3(b). The proportions between the minor radius and the major radius are set by the *aspect ratio* R_0/a, and different ratios give different environments to study.

When charged particles flow in the magnetic chamber, they are not allowed to explore the whole space freely: the magnetic field affects the velocity orthogonal component constraining the particles to move in their Larmor orbits, around the so-called guiding centre, while the parallel component is not affected. Therefore, particles follow an helical path around field lines, as shown in Fig. 1.3(a).

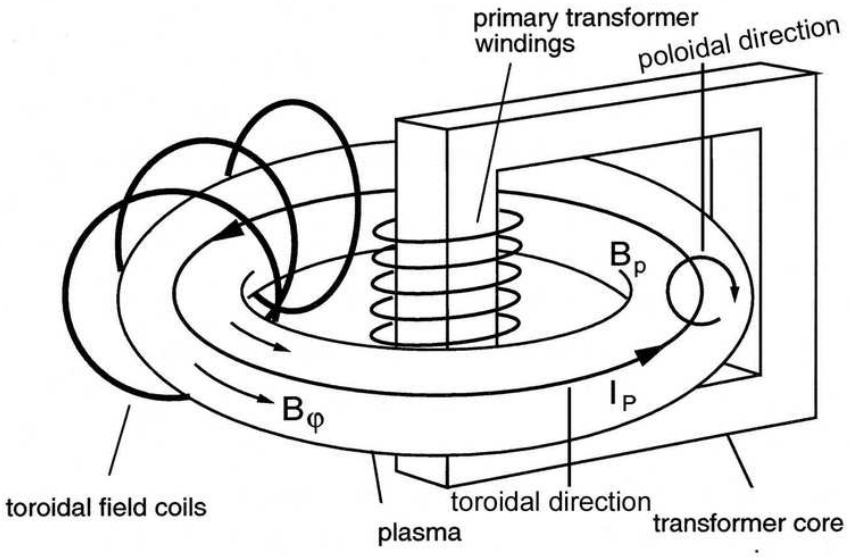

Figure 1.4: Representation of transformer-like behaviour of a tokamak.

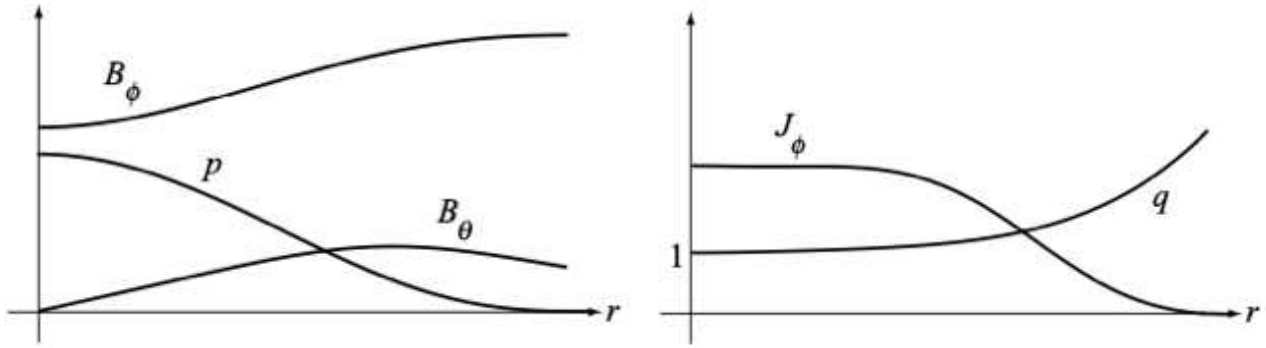

(a) (b)

Figure 1.5: Typical profiles in a tokamak in the large-aspect-ratio limit $R_0/a \to \infty$

Magnetic field lines in toroidal experiments have both a poloidal component, B_θ, which is mainly generated by the toroidal plasma current I_P, and a toroidal component, B_ϕ, which is usually produced by currents flowing in external conductors. Toroidal current by itself can be driven in many ways, but the main mechanism relies on current induction as in a transformer. For instance every tokamak behaves as a giant transformer, where coupling takes place between the central solenoid, acting as the primary circuit, and the toroidal plasma current, acting as the single secondary current turn, as shown in Fig 1.4.

The characteristic poloidal and toroidal magnetic field profiles in a tokamak are illustrated in Fig. 1.5(a). Note that, the toroidal magnetic field has a slight diamagnetic dip, which is responsible for holding the plasma in radial pressure balance by the pinch effect.

Having two components, magnetic field lines are thus helixes which wind around the torus. These lines close on them self and a set of them defines a so-called *magnetic surface*. Magnetic surfaces are nested one into another, and their shape and dynamic behaviour is established by the plasma regime and defines their topology. Fig. 1.6 shows an example of magnetic surface topology.

Helical magnetic field lines are described by the so-called safety factor, q, which is defined as the ratio between the angular distance a field line has to toroidally travel before reconnecting, hence

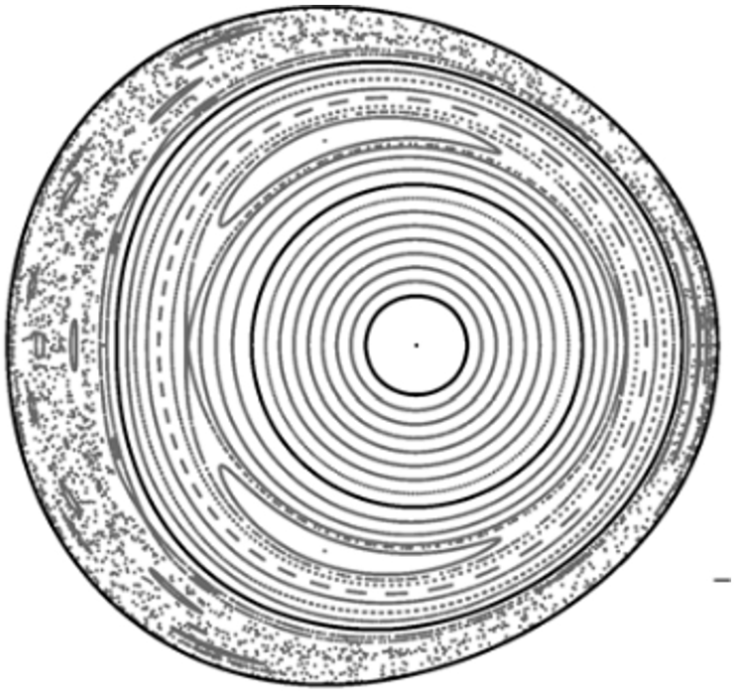

Figure 1.6: Sketch of nested magnetic surfaces on a poloidal plane for different topologies. From inside to outside: Ideal MHD, resistive MHD, ergodic plasma.

completing a full poloidal turn. It can be linked the torus radii and the magnetic profiles as:

$$q(r) \approx \frac{rB_\phi(r)}{R_0 B_\theta(r)} \tag{1.9}$$

where R_0 is the torus major radius. A typical profile of the safety factor is shown in Fig. 1.5(b). The name safety factor comes from the fact that this quantity is crucial to determine several features of the plasma instabilities.

1.1.3 ITER

The International Thermonuclear Experimental Reactor (ITER) represents the biggest hope in the future of fusion energy. It is currently being built in Cadarache, Southern France. It is an international collaboration between the biggest economies in the world, namely the EU, China, the USA, South Korea, Japan, India and Russia.

ITER combines in its design the biggest achievements in fusion physics and engineering, from super powerful superconducting coils to ensure long lasting plasma discharges, Beryllium first walls and Tungsten Divertor to ensure less impurity pollution and lower fuel retention eventually leading to higher performances, D-T reactions and high Q values well above 1.

ITER will offer the possibility of studying several reactor relevant scientific and technological issues, which are beyond the present experimental capabilities. In addition it is by far the biggest fusion experiment, overtaking JET as the most advanced tokamak on the planet. Fig. 1.7 shows the comparison between ITER and JET sizes, while table 1.1 presents desired working ITER parameters.

1.2 The danger of plasma disruptions and their mitigation: the Shattered Pellet Injector

The dynamic of the plasma and its interaction with the external environment is usually described in the framework of the *Magnetohydrodynamic* (MHD) theory, a model where the plasma is treated as one single fluid [TokW].

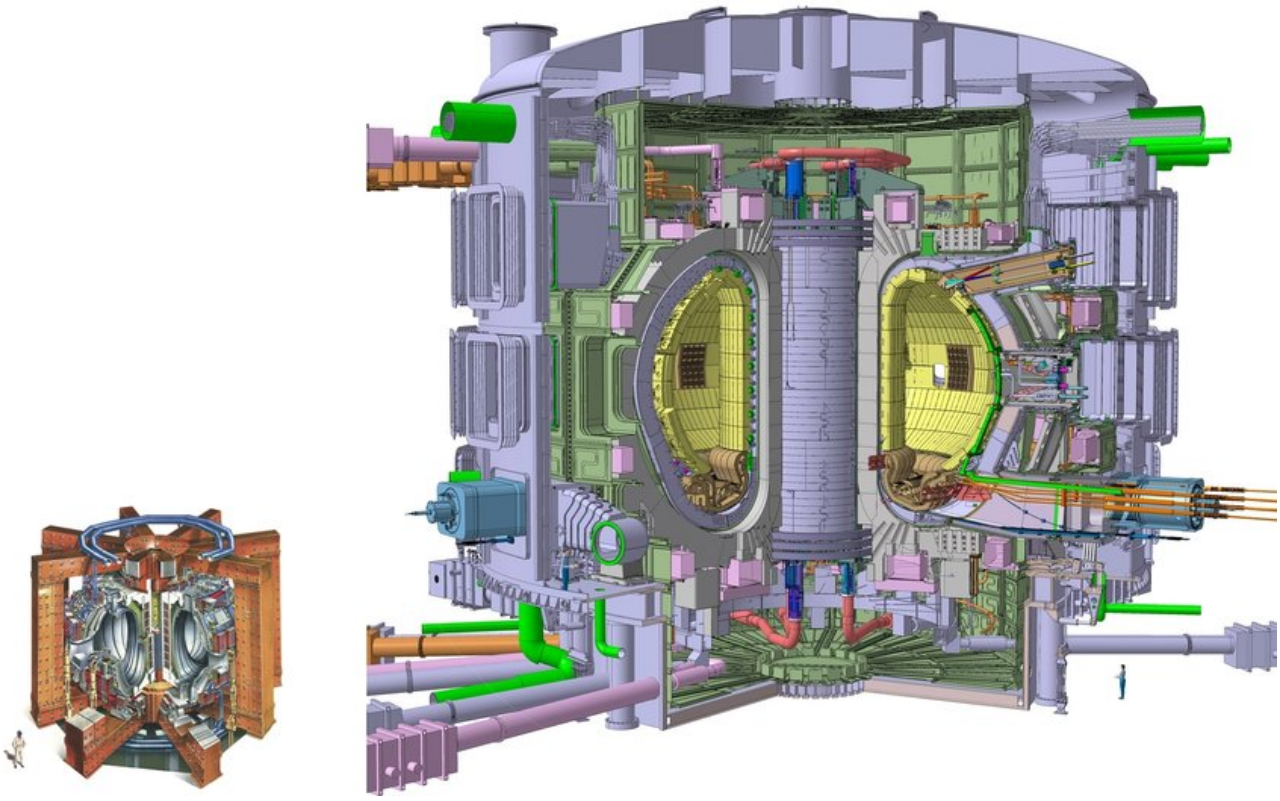

Figure 1.7: Comparison between JET (bottom left) and ITER (right) dimensions. A person is shown for scale next to both machines.

ITER Parameters	Value
Major Radius R_0	6.2 m
Minor Radius	2 m
Toroidal field at R_0	5.3 T
Plasma Current	15 MA
Average Electron Temperature	8.8 keV
Combined Heating Power	40 MW
Fusion Power	500 MW
Burn time	$\geq$ 400 s
Fusion Gain Q	10

Table 1.1: Main ITER parameters.

In this context, several instabilities can be observed and described, such the as kink modes, which cause bending and squeezing of plasma column, tearing modes, which alter the magnetic topology and many others.

In this Thesis work a non rotating tearing mode, the *locked mode*, has been encountered when analysing the plasma experiments. The locked mode is a violent instability and the prevalent cause of a dramatic plasma termination called *disruption* [Vries11]. Disruptions are plasma events characterised by very faster temperature collapse, of the order of 1 millisecond, and fast plasma current terminations, of the order of tens of milliseconds. These two phases are respectively called Temperature Quench (TQ) and Current Quench (CQ).

During both the collapses, the plasma thermal and magnetic energy plummets to zero, hence by energy conservation these energy contents must be transferred to something else. In a disruption event, the thermal energy is conducted to the vessel walls, while magnetic energy is converted to large eddy currents in the vessel.

Disruption events thus are able to locally melt first wall components through massive heat loads and high-energy beams of runaway electrons; in addition mechanic stress are applied on the machine itself through electromagnetic forces. The device can be seriously damaged and any accident can lead to weeks of integrity checks and a lot of money in the process. Moreover, heating systems and the whole diagnostic package can be harmed. Finally, even if unmitigated disruption events happen and damages are fixed, there's a limit on the stress the machine can hold before it is no longer good enough to work or just in need of decommissioning.

This is a very serious problem for the whole fusion community since every machine is uniquely designed and any loss is a huge loss, both in scientific and financial terms. Needless to say that in the prospective of a running power plant a disruption puts everything on hold until a stable plasma can be formed again. This event has to be avoided to all costs in order to provide a steady and reliable energy output.

All of disruption consequences can seriously damage the device, therefore mitigation systems were developed in order to easy the inevitable loads the machine is subjected to. In the following section the most promising protection system is presented.

1.2.1 The Shattered Pellet Injection mitigation system

ITER, as reported in Section 1.1.3, is the next big experiment in the field, the biggest ever and huge expectations are surrounding the project. This is a particularly massive and accurate machine which embodies many important engineering and fusion physics achievement of JET and many other devices in its design. This makes it very complicated and delicate at the same time.

If disruptions are dangerous for any machine, they are nearly as lethal for ITER: its large dimensions, currents and stored energy are gigantic and any load from a disruption could be catastrophic for the experiment; it is said that only a few tens of unmitigated disruptions are accepted in its 20+ years lifetime, hence 1-2 a year maximum, setting a very high stability threshold on the daily multiple pulse regime scientists want to set. In any case even that once a year given event should be avoided if operations are to be kept on going, otherwise the whole machine has to be checked for damages and this can take a lot of time.

To design a robust and reliable Disruption Mitigation System (DMS) for ITER, over the years a series of disruption protection systems have been designed, manufactured and tested in several magnetic fusion devices. The main ones are the Massive Gas Injection (MGI) and the Shattered Pellet Injector (SPI).

MGI and SPI systems are both disruption mitigation systems based on the injection of Deuterium and/or mixtures of Deuterium and Noble gases deep into the plasma column. Exploiting a fast and massive injection of impurities, the plasma is able to relax through radiation its inevitable energy release.

The main difference between the two systems is the state of the injected substance: for the MGI we have gases (Massive Gas Injection), while for the SPI a frozen pellet is shot through a pipe and shattered right before the entrance of the vacuum vessel.

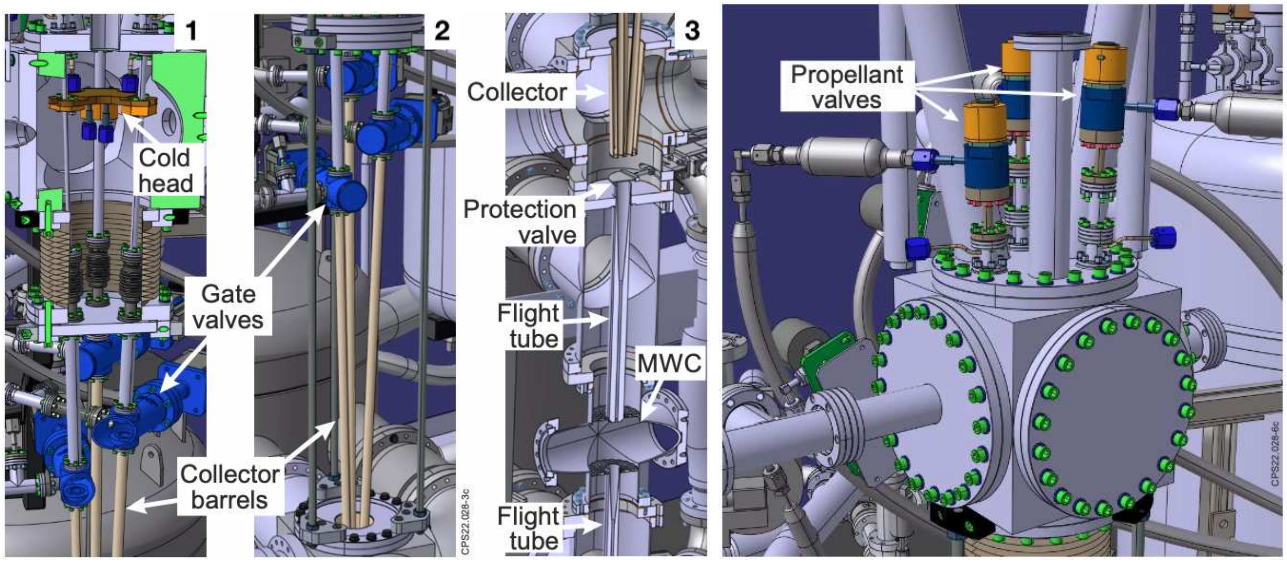

(a) (b)

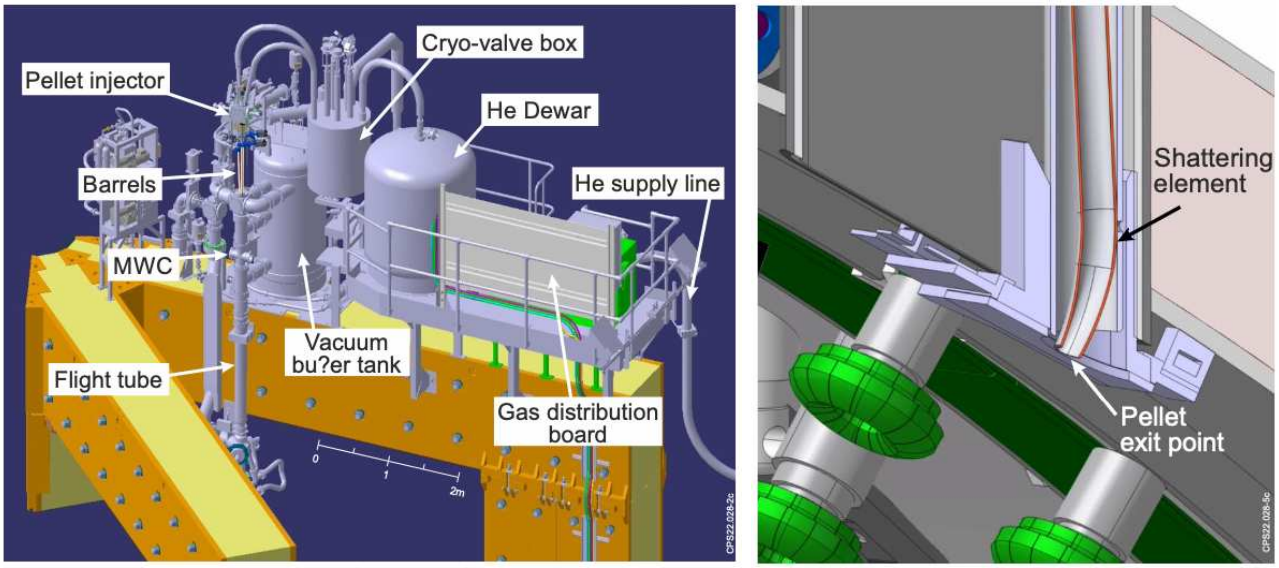

(c) (d)

Figure 1.8: (a) Triplet of images showing all the components the pellet flies in and relative names. (b) Particular of the propellent valves and cold head box (metal cube). (c) Overview of pellet injector and SPI cryogenics installed on one of supporting cranes. (d) Final section of the flying tube, shattering element and pellet exit point.

Both the techniques have pros and cons, but at the moment the SPI is considered the preferred method between the two due its ability of reaching the deep hot plasma core quicker. Its performance has shown to better mitigate thermal loads onto the divertor respect to the MGI system, while its delivery design is hardly affected by geometry features [Commaux16]. These characteristics are fundamental for a machine like ITER, which cannot afford unmitigated disruptions.

MGI sensitivity toward implementation geometry arises from its weak impurity delivery and penetration in a in ITER-like dimension environment; strong neutron and gamma rays fluxes impose large distances between the vessel and the MGI, resulting in a drop in density and pressure of injected gas, eventually causing worse particle assimilation [Commaux16]. Such a problem is not present in SPI, since frozen pellets can be shot from far away and shattering occurs very close to the plasma edge; therefore it only a matter of tuning the firing time for a longer travelling distance. At present, the SPI is the main DMS in ITER.

The *Joint European Torus* (JET), located in Culham, Oxfordshire (UK), has devoted over the years several experiments to disruption mitigation. Firstly hosting the Massive Gas Injection (MGI) system [Lehnen15], JET has now been equipped with an SPI system.

JET is in a broad sense ITER test ground, and thus suitable for this kind of study. It is the device closest in dimensions and currents to ITER and it is equipped with a single Tungsten divertor at the bottom while the inner and first wall are covered in Beryllium tiles, as ITER. Basically all the experimental campaigns ran at JET after the last upgrade (2011) had the intention to acquire knowledge in how a system like ITER would work and how a tokamak device could be improved before ITER get started. That's why JET scientists are running SPI experiments: it will give the closest result to a ITER like scenario.

In the following, the JET SPI system, used in the experiments analysed in this thesis work, is reported.

Physically the JET SPI system can be divided in 3 sections:

- *Pellet formation and injector*: The SPI is equipped with three different barrels (named A, B, C) which are characterised by a different diameters d, hence a different pellet mass, and length/diameter ratio l/d, see 1.8(a)[2]. Depending on which barrel is currently used, the pellet is formed in a different location in the cold head (Fig. 1.8(a)[1]) , where the pellet is produced; the shooting system relies on propellent valves and/or electromagnetic coils (Fig. 1.8(b)) in order to accelerate the pellet by a mechanical punch (coils) or pressure release (valves) [Gerasimov22]. Above the supporting crane, the cryogenics and pressure systems needed to freeze the pellet have been installed. See Figs.1.8(c)

- *Microwave camera and flying tube*: Once departed, the pellet flies through the gate valves, then through the collector which directs the pellet into the flying tube (Fig. 1.8(a)[1]-[2]). Here the pellet needs to be scanned to check its integrity, therefore a microwave cavity is installed along the tube, as shown in Fig.1.8(a)[3]. How the microwave cavity works is explained in chapter 2, Section 2.7.

- *Shattering element and the exit point*: The last stage before plasma is the shattering element, which is simply a kink in the flight tube, around 28.4° respect to vertical, on which the pellet crashes and shatters in thousands of pieces [Gerasimov22]. The details of the shattering element is shown in Fig.1.8(d). Finally the plume passes through the exit point and mitigation can start.

In the analysis presented here only B barrel pellets were used, whose characteristics are the following: $d = 8.1mm$, $l/d = 1.6$ [Gerasimov22].

Fig. 1.9 shows a wide image of the inside vessel of JET and many of its components (and associated acronym) and the SPI pellet trajectory. It is important to note that JET is equipped with a single pellet injector.

1.2.2 The importance of Radiation Asymmetry investigation for ITER

The scope of a plasma mitigation system is to ease, during an inevitable disruption, the thermal and electro-magnetic loads the device is subject to to avoid first wall melting and critical mechanical

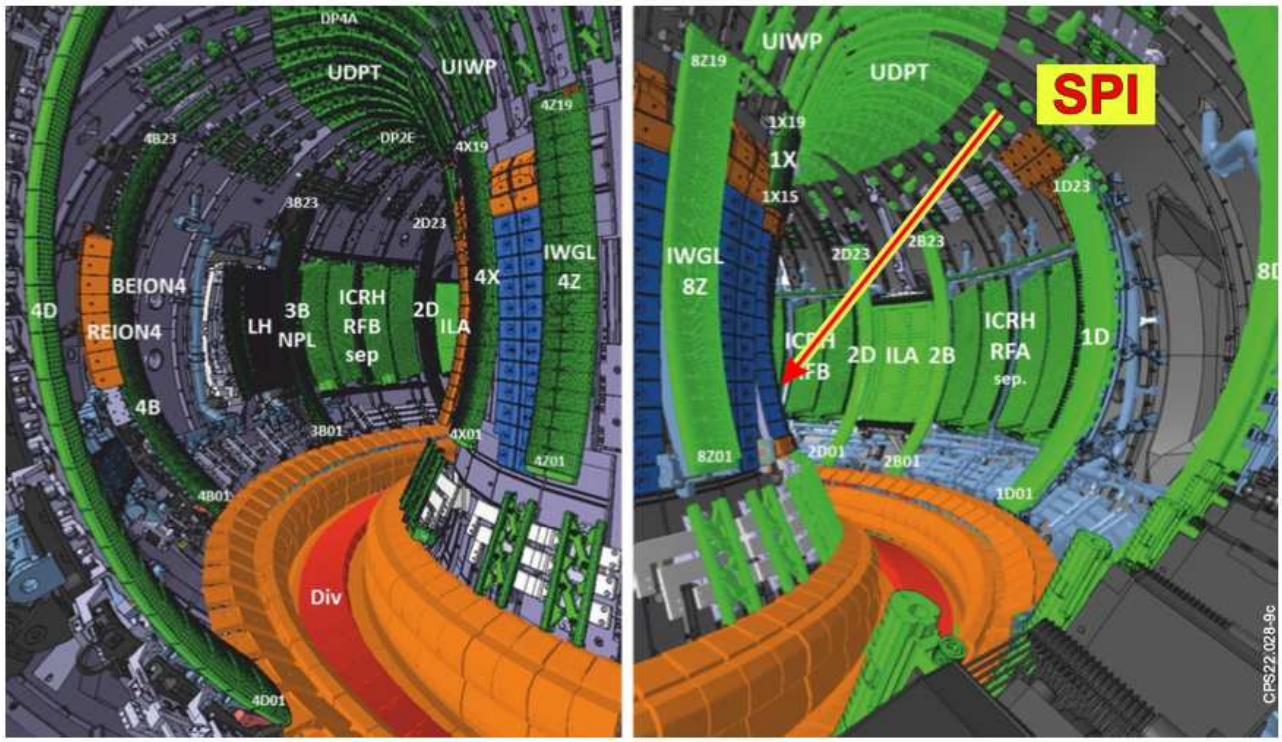

Figure 1.9: Some of JET vacuum vessel components and diagnostics (and relative acronyms) view. SPI location and trajectory is shown as well.

strains which could stop operations for a long time. The way developed with SPI focuses on introducing radiation as one more method for the stored energy to be released during a disruption, in particular during the TQ.

When the SPI system is used, the plasma radiation peaks usually near the injection location since impurity density is at its highest there: the radiation is inevitably not symmetrical along the toroidal angle and difficulties start to arise as the more asymmetric the radiation distribution gets. Strong asymmetries lead to a more localised power deposition in one position respect to another, and this might cause local first wall melting by itself. In fact, radiation can reach levels around a few GW and such a power deposition on a small surface needs to be avoided. It is obvious that such a scenario completely misses SPI's purpose in first place.

This Thesis work aims at investigating which is the radiation asymmetry content when a disruption is mitigated in JET and understand its toroidal distribution in a ITER like wall environment, in order to give ITER quantitative predictions if a disruption happens in one of its campaigns. We must stress on the fact that ITER is the key to unlock many open issues towards the exploitation of fusion as a viable energy source and we cannot afford the machine to be damaged.

Chapter 2

JET and the main plasma diagnostics

In this chapter, JET device and its capabilities are described, together with the main diagnostics involved in this work: bolometry, saddle loops, Electron Cyclotron Emission (ECE), polarimeter, microwave cavity diagnostic and optical fast cameras.

2.1 Brief description of JET

JET, the Joint European Torus, is currently the largest running fusion experimental tokamak on the planet. From its completion in 1983 JET has seen many upgrades, among which the most remarkable being in 1993-1994 when the divertor was added and in 2011 when the ITER-like wall (ILW) beryllium and tungsten components were installed.

JET's design is based on a toroidal D-shaped vacuum chamber, with a major radius R= 2.96m and characteristic D-shaped cross section dimensions of 4.2m and 2.5m. Its structure is composed of the toroidal and poloidal field coils, the vacuum vessel and its supporting mechanical structures and the transformer core limbs. A design sketch of JET is shown in Fig. 2.1, while its dimensions in Fig 2.2.

The toroidal magnetic field is produced by 32 D-shaped coils enclosing the vacuum vessel, while the main poloidal field coil is wound around the central column of an iron transformer core, acting as the primary of the transformer. Six other poloidal coils are optimally placed to provide control of the plasma shape and position. Fig. 2.3(a) and Fig. 2.3(b) show the toroidal and poloidal field coil systems installed on JET, respectively.

JET Parameters	Value
Major Radius R	2.96 m
D-cross section lengths	2.5 m / 4.2 m
Toroidal field	3.4 T
Plasma Current	5 MA
Plasma Volume	90 m^3
Electron Temperature	10 keV
Combined Heating Power	38 MW
Record Energy Release (2021)	59 MJ (10MW >4s)
Record Power Release (1997)	16.1 MW

Table 2.1: Table of JET main dimensions and plasma parameters.

The main plasma parameters and JET results are collected in table 2.1.

2.2 Error Field Correction Coils

Error Field Correction Coils (EFCCs) are a set of coils typically installed in tokamak devices. As the name suggests, they correct error fields, which are spurious magnetic field perturbations. These

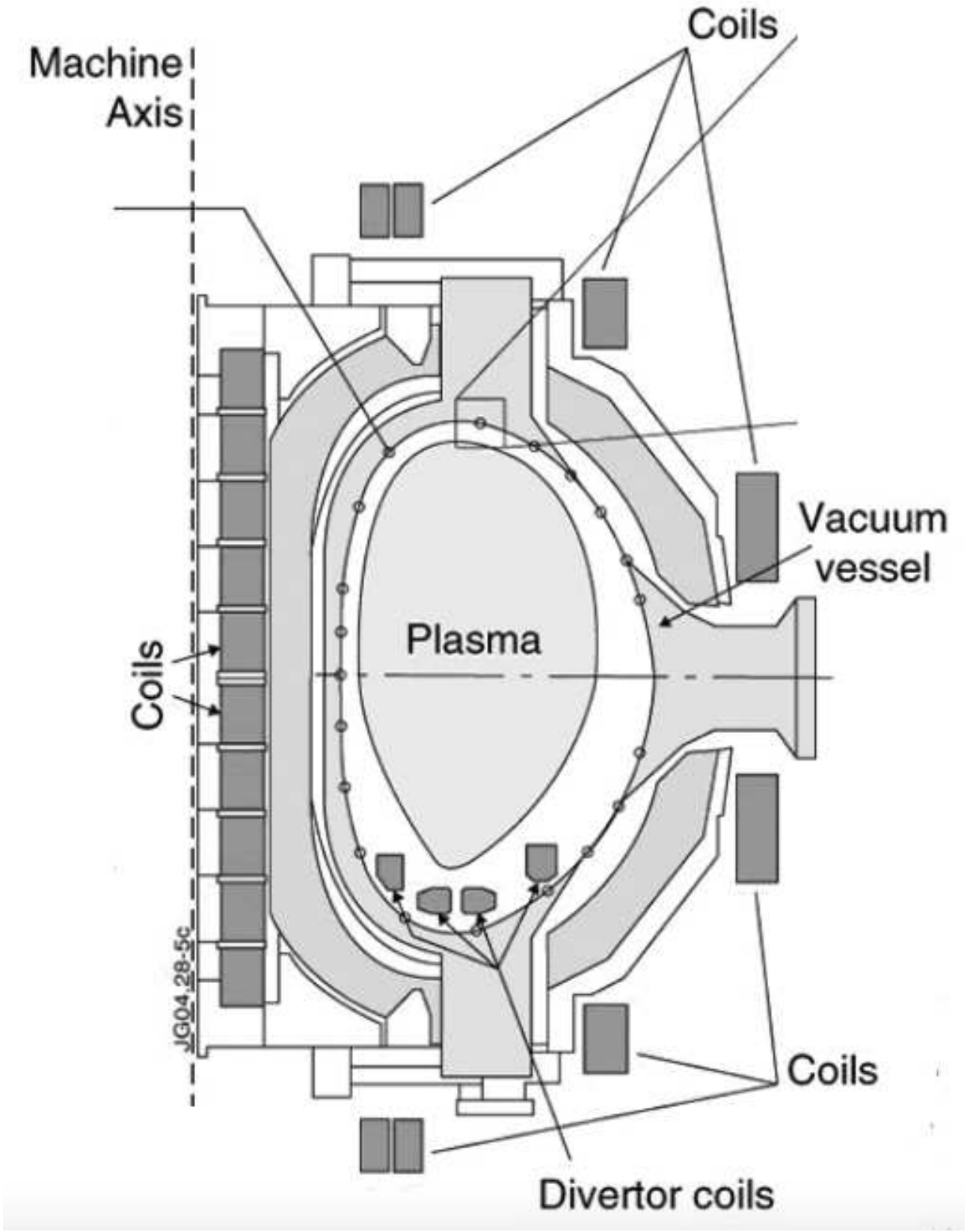

Figure 2.1: Sketch of JET poloidal section.

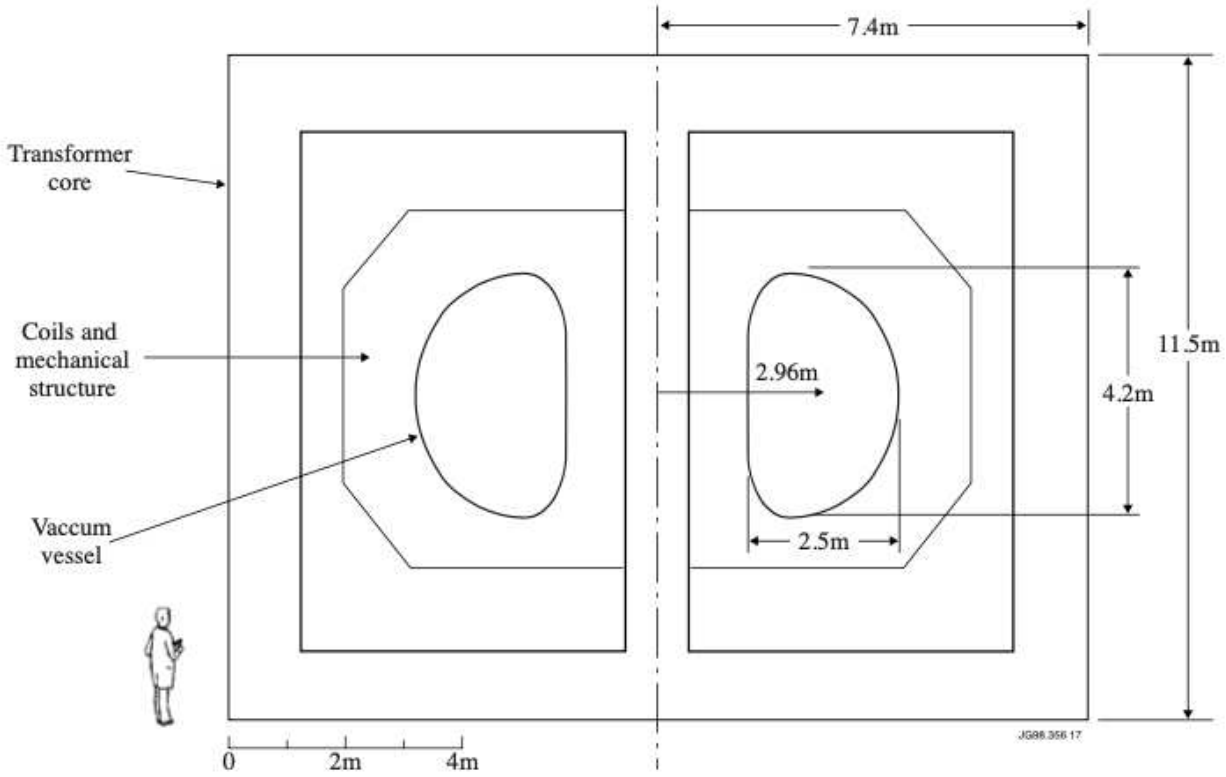

Figure 2.2: Dimensions of JET.

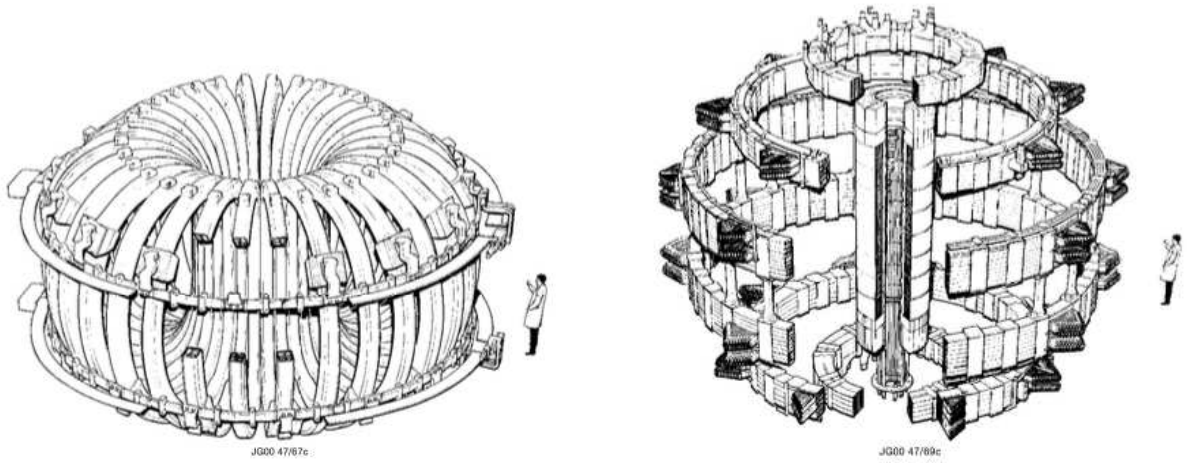

(a) (b)

Figure 2.3: (a) Toroidal and (b) poloidal field coils in JET.

perturbations can arise from a number of reasons: misalignment introduced in the construction of the device, imperfections in the manufacture of the field coils, 3D structures in the wall surrounding the plasma, current feeds or presence of ferromagnetic materials near the plasma surface, etc [Strait15]. [Gambrioli22].

Error fields are particularly detrimental for plasma stability as they can trigger MHD instabilities, especially at the $q = 2$ resonant surface, degrading particle and energy confinement [Callen11].

JET is equipped with 4 EFCCs, each spanning 70° in the toroidal direction and with a radial distance of 5.3 m to 7 m from the axis of the machine. The EFCCs are arranged symmetrically around the vacuum vessel and external to it. A sketch of the EFCCs system is shown in Fig 2.4. The coils are located in octants 1, 3, 5 and 7 of the vessel; each coil has 16 turns and it carries a maximum current of 6 kA in a single turn.

The EFCCs can be wired in n=1 and n=2 locked mode configurations. The n=1 configuration, used in the experiments presented in this work, is induced by feeding EFCCs 180° apart with oppositely directed currents. The induced magnetic field perturbations can have various toroidal phases, by varying the EFCC current polarities in the quadrature pairs of coils.

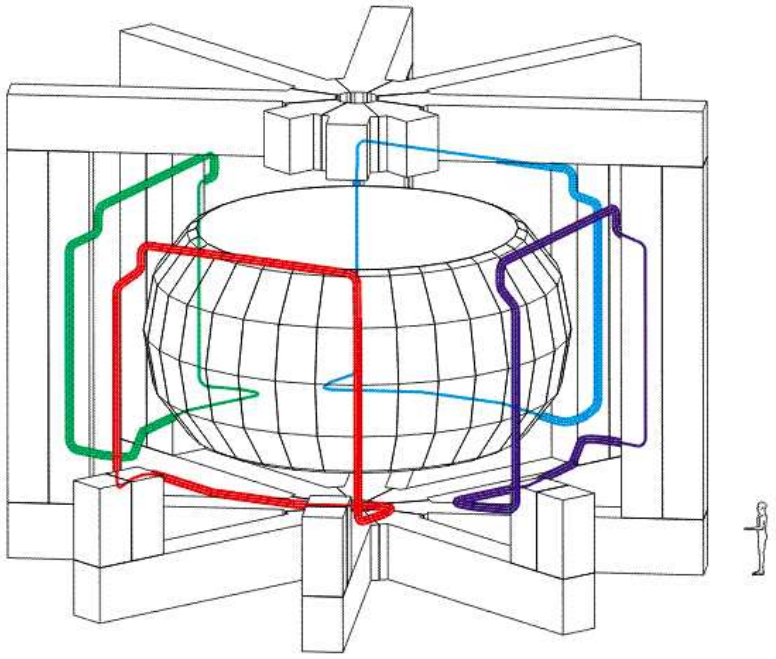

Figure 2.4: EFCC coils installed on JET.

During SPI experiments analysed here, the EFCC system has been exploited to trigger a n=1 locked mode, which is a magnetic island fixed at a certain toroidal position [TokW], [Hender07]. Fig. 2.5 shows the geometric configuration of a n=1 locked mode. The locked mode is characterised by its intensity, i.e. the n=1 radial magnetic field amplitude, and the toroidal position of the O-point of the established magnetic island. Both quantities can be calculated by analysing saddle coil measurements, as will be described in the next section.

The locked mode can grow in size, destabilising the current radial profile and destroying the nested magnetic surface geometry. In this case, the magnetic field lines become ergodic, i.e. they do not lie on nested flux surfaces any more but fill the whole volume, degrading confinement and eventually may resulting in a disruption.

It has been documented that a majority of natural disruption events in JET is due to the presence of a n=1 locked mode [Vries11]. This justifies why the EFCC system have been adopted in radiation asymmetry experiments: the EFCCs are able to control the locked mode dynamics and in particular its phase, mimicking the physical precursor of a disruption. However, since a systematic investigation of the SPI dynamics in a simple plasma environment is desired, mode locking is monitored in such a way as *not to trigger* substantial magnetic island growth, that could lead to a real disruption.

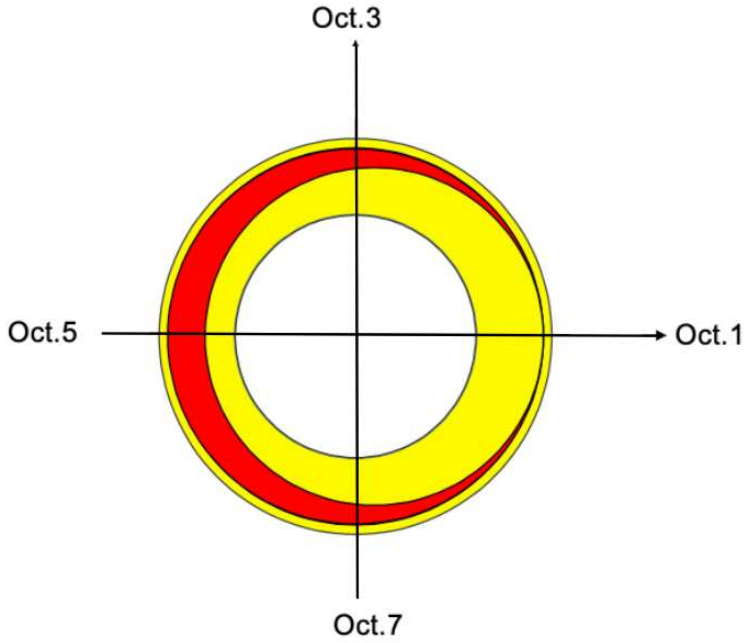

Figure 2.5: Sketch showing a n=1 magnetic island (red semi-moon) in the plasma (yellow).

2.3 Magnetic diagnostics: Saddle Loops

Magnetic diagnostics are fundamental tools in order to understand what is happening inside a magnetic fusion device: they provide information about plasma current, toroidal and poloidal magnetic fields, plasma shape, loop voltage, magnetic surfaces profile, q-profile, magnetic perturbations and much more. Therefore it is possible to reconstruct main equilibrium features as well as important MHD activity. The principle of observation of magnetic diagnostics always relies on Faraday's induction law.

In this Thesis work the main interest was toward saddle loops. JET is equipped with 8 sets of 18 independent wire loops installed along each of the octant's external frame, hence covering the whole external surface of JET. Fig. 2.6(a) shows the position of the saddle coils along the poloidal direction in a particular octant.

By linearly combining signals of saddle coils 180° apart, i.e. placed in Octants 1-5 and 3-7, one can obtain the Sine and Cosine components of the n=1 radial magnetic field amplitude associated with a locked mode, making possible the calculation of the amplitude and phase of the locked mode. Such loops are presented in Fig. 2.6(b).

2.4 Bolometers

Bolometers are a particular set of diagnostics that measure electromagnetic power from the plasma. Nowadays different types of bolometers can be found (thermic, pyroelectric...), but metal resistive (thermic) bolometers represent the most solid tool of power measurement in the context of large machines such as JET [FP]. Bolometric diagnostics represent an essential tool for JET power detection. From divertor radiation to disruptions, bolometers help understand how much electromagnetic power is released in the machine at any given time, allowing energy measurement as well.

A typical metal resistive bolometer works in the following way: radiation is absorbed by a thin and highly conductive metallic foil thermally coupled with a thermal reservoir which is used as thermal reference. When radiation is deposited onto the absorbing metal, it is heated up. Therefore it is possible to get an accurate estimation of the absorbed, thus emitted, electromagnetic power by measuring the change of the resistivity of the absorbing metal. The ratio of the capacitance C to the absorber and the thermal conductivity λ between the absorber and the reservoir is the intrinsic time constant of the bolometer, i.e. $\tau_C = C/\lambda$. This defines the temporal resolution of the bolometer.

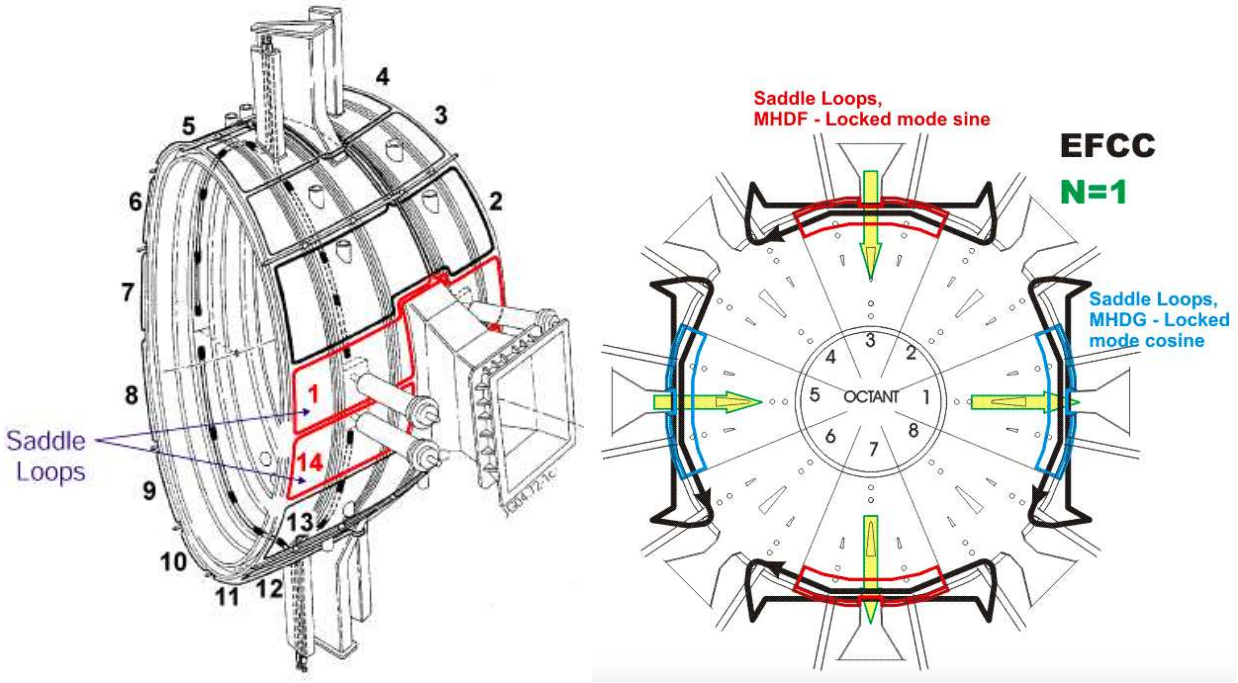

(a) (b)

Figure 2.6: (a) View of a particular octant showing the geometrical configuration of saddle loops. As can be seen, these loops cover the entire octant surface. (b) Saddle loop location for n=1 MHD mode detection. Plan view.

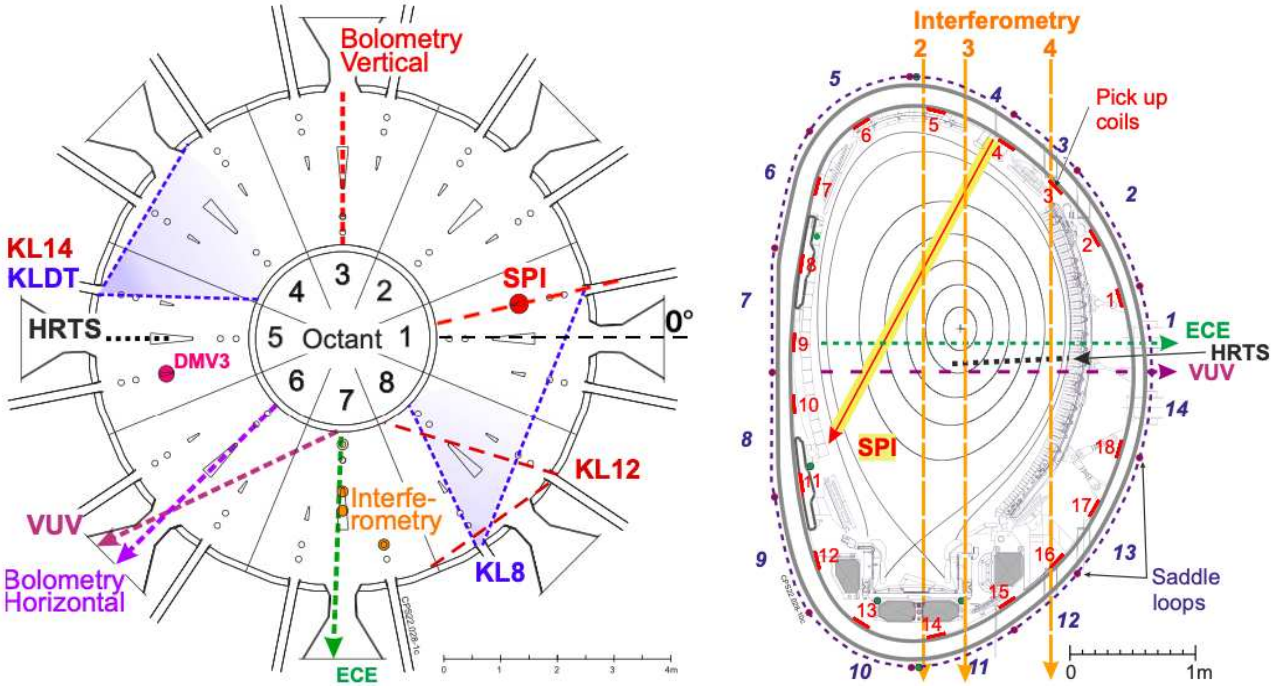

(a) (b)

Figure 2.7: Toroidal (a) and poloidal (b) view of some JET non-magnetic diagnostics and their location. SPI location is highlighted in (a), while in (b) we see the pellet line of fire from barrel exit. From (a) we have: SPI, fast visible (KL8 and KLDT) and infrared (KL12 and KL14) camera views, bolometry, interferometry, ECE (electron cyclotron emission), VUV (Vacuum UV spectroscopy), HRTS (high resolution Thompson scattering) and DMV3 (Disruption mitigation valve), while from (b) we can see pick-up coils and saddle loops apart from those already mentioned.

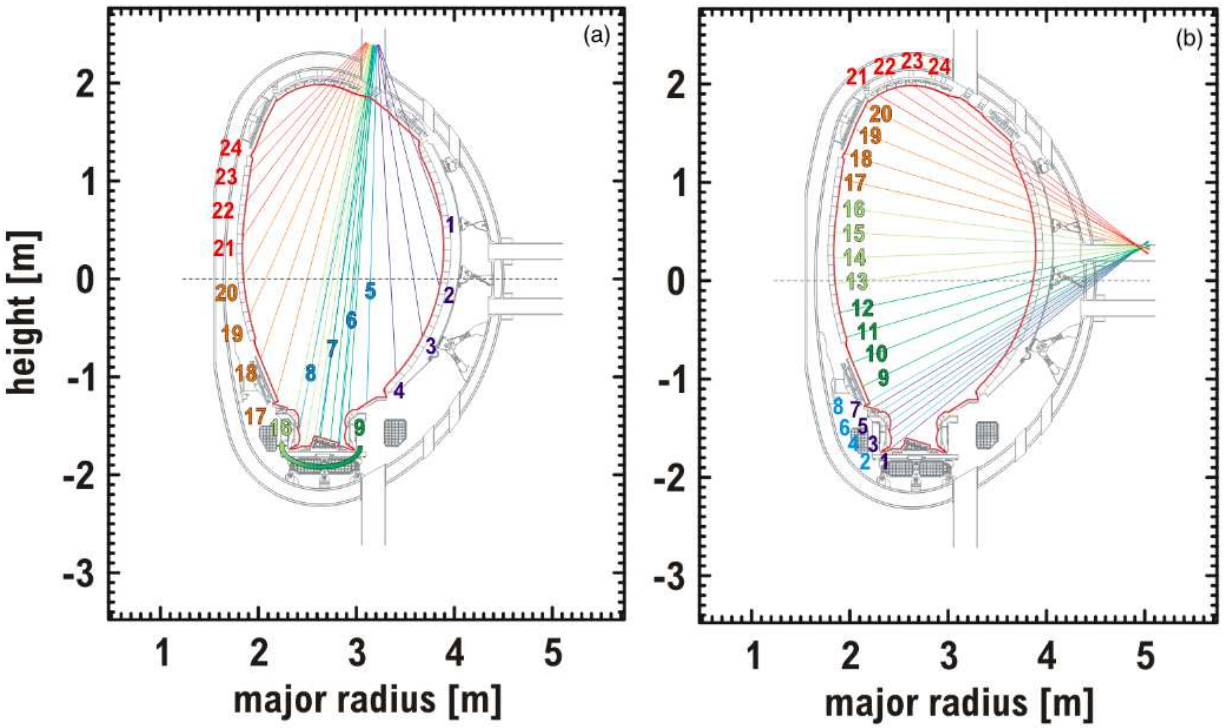

(a) (b)

Figure 2.8: Poloidal cross section of the JET machine with (a) Vertical bolometer diagnostic fan loaded in Octant 3 and (b) Horizontal bolometer diagnostic at Octant 6. Each bolometer has 24 line of sights, allowing the whole set to cover the entire cross section of the plasma. Note that in the divertor region spatial resolution is higher.

JET is equipped with two bolometer sets, one designed to collect "horizontal radiation" and the other for "vertical radiation", respectively at $\phi_H = 225°$ and $\phi_V = 90°$ with respect to the designated origin on Octant 1. Each bolometer consists of 24 channels of single bolometer heads, each facing a slightly different direction in order to cover the whole poloidal section of the plasma. Fig. 2.8(a) and Fig. 2.8(b) show the vertical and horizontal line of sights, respectively, while Fig 2.7(a) shows the bolometers toroidal location.

2.5 Electron Cyclotron Emission

The Electron Cyclotron Emission (ECE) diagnostic is based on the cyclotron radiation emitted by the electrons during their gyration around the magnetic field lines. The frequency depends on the strength of the magnetic field, hence on the position in the plasma. Moreover it is independent of the electron's energy, which affects the strength of the emission only.

In the context of JET, the electron cyclotron emission is exploited to retrieve the electron temperature along the minor radius of the torus. Once the magnetic field profile is known, it is possible to calculate the expected ECE frequency of electrons at that radius. If then a microwave detector is tuned to that frequency, its output amplitude can infer the temperature of the electrons there. A suitably tuned multi-channel array of detectors covering the band of emissions of a given magnetic profile, can give the electron temperature over the whole radius. This is the operating principle of the ECE diagnostic.

The JET ECE system has 96 channels, each correlated to a frequency, hence a position along the minor-radius. However, if the magnetic profile is not radially monotonic, the radial position for a given frequency may be ambiguous. The ECE radiation is collected from the tokamak low field side as can be seen in Fig. 2.7(b), perpendicular to the magnetic field along the major radius. The antenna is located in Octant 7 (Fig.2.7(a)) at a height of Z=0.248m. Since for typical JET configurations the centre of the plasma respect the height of the antenna is displaced upwards by typically 0.3 to 0.4 m, in general the exact plasma centre is not accessible by the radiometer. The time resolution is typically

0.5 ms and can reach up to 0.2 ms to study faster events such as disruptions.

2.6 Polarimetry

To measure plasma density, the main diagnostics used are the High Resolution Thompson Scattering (HRTS) and the interferometer. Unfortunately, for disruption dynamics, the temporal resolution of both systems is not high enough, hence polarimetry was considered.

Polarimetry exploits the so-called *Faraday rotation* effect: when polarised light waves travel in magnetised plasmas, the angle of polarisation suffers a rotation induced by the local parallel component of magnetic field and local electron density. The formula giving the relation between the polarisation angle change and plasma quantities is the following:

$$\Delta\theta = C \int_{\gamma} n_e \, \mathbf{B} \cdot d\mathbf{l} \tag{2.1}$$

where C is a constant and γ is the integration line, n_e is the plasma electron density profile and $\mathbf{B}$ is the plasma magnetic field. The dot product $\mathbf{B} \cdot d\mathbf{l}$ gives the parallel component of $\mathbf{B}$ along the integration path.

Measuring this angle difference over a certain distance then gives the line integrated density when the magnetic field profile is known. Assuming the poloidal magnetic field reconstructed by other means, it is thus possible to measure the line integrated electron density along a given line of sight in the poloidal cross section. The JET polarimetry shares the instrumental equipment with the interferometry, shown in Fig. 2.7(b). For disruption purposes core density was needed, therefore only the line of sight "3" was considered, providing 1ms time resolution across.

2.7 Microwave Cavity

The microwave cavity (MWC) diagnostic provides information on the pellet integrity in the flying barrel once it has been launched. For instance, pellets can unexpectedly break right after being shot (breakage probability is correlated to firing method, mechanical punches tend to break pellets more than pressure discharges [Gerasimov22]) and knowledge of that is crucial for mitigation success in JET and in ITER.

The instrument consists of a passive resonant cavity whose resonant frequency changes when the dielectric pellet material passes through it. Pellet path in the cavity structure is shown in Fig. 2.9. The resonance change is proportional to the mass of the pellet [Gerasimov22], hence a proxy of the mass of the pellet can be obtained from the analysis of MWC signals. The number of peaks in the signal is the number of detected pieces in the cavity.

Since the microwave cavity centre is located 4722 mm away from the barrel exit point, it can happen that a pellet breaks mid-flight after being scanned by the cavity but before shattering; this thesis contains such cases and it is possible to infer the intactness of the pellet before shattering by looking at the fast camera video of shards arrival in the plasma. As will be shown later in the thesis, those data points related to broken pellets are well distinct from "good" pellets, i.e. pellets whose integrity persisted until the shattering point. Examples of an intact and a broken pellet from microwave cavity and fast camera pictures are shown in Chapter 3, Fig. 3.3 and Fig. 3.6(a) respectively.

2.8 Fast Visible Cameras

JET is equipped with two wide-angle, high-speed visible wavelength cameras: KL8-E8WA (Oct 8 looking towards Oct 2) and KLDT-E5WE (Oct 5 looking towards Oct 2), as shown in Fig. 2.10. Both cameras have wide-angle tangential views of the JET plasma from just below the horizontal mid-plane but KL8 has a direct view of the SPI, making it a crucial tool for in-plasma shot analysis during the considered radiation asymmetry experiments. This is because KL8 can provide information about the injection timing and particle assimilation of SPI. Typical frame rates of 10 – 20 kHz were used for

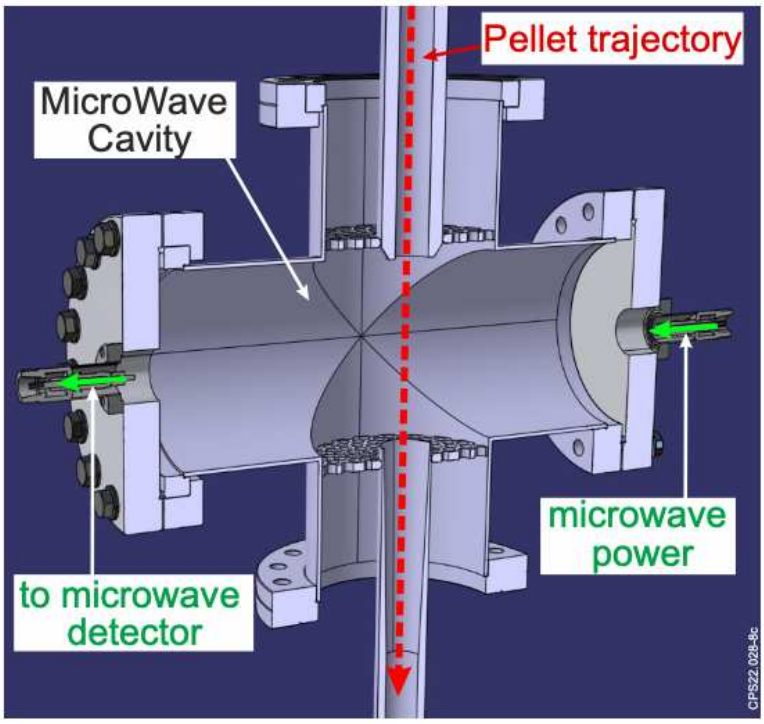

Figure 2.9: Microwave cavity vertical cut-through. Example of a pellet trajectory (dotted red line) is shown.

SPI experiments, with exposure times (frame duration) in the range of 1μs - 100μs to obtain optimal signal levels. KL8 is equipped with remotely interchangeable narrow band filters to image spectral lines of Ne atoms (692.9 nm), Ar atoms (706.7nm) or Ar+ ions (611.5 nm). During this work only visible band filters were used.

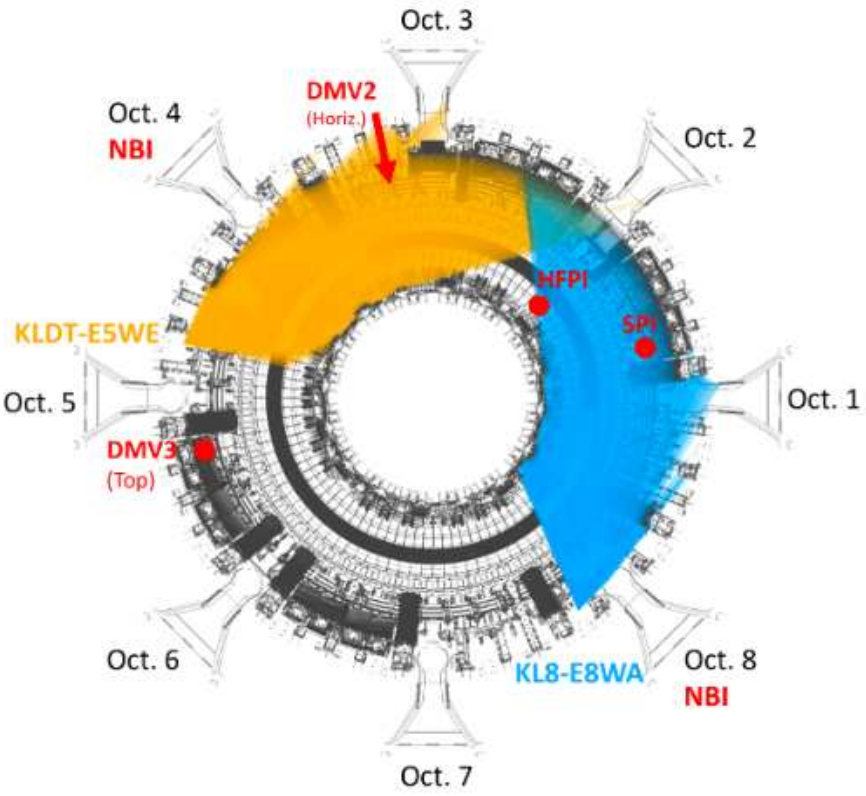

Figure 2.10: Top view showing fast camera coverage of the torus. Note that SPI is monitored by KL8-E8WA camera.

Chapter 3

Plasma events during SPI experiments

In this chapter the plasma scenario used in the SPI experiments analysed in this thesis is presented. In particular, the chain of events leading to the thermal quench and the current quench is described in details.

3.1 Chain of events leading to thermal and current quench

As introduced in Section 1.2.1, the SPI system is designed to be a disruption *mitigation* system, i.e. it makes possible for the stored energy in the plasma to be relaxed in a safe way, limiting the possible dangerous loads onto the vessel wall. However, the experiments under investigation have been performed on a "healthy" non-disruptive plasma scenario, and SPI is used *to trigger* a disruption event, not to mitigate it *if it occurs*. This allows to investigate the effects of SPI on the plasma and to better understand the underlying physics in a more controlled and systematic way. These studies allow to reinforce the use of the SPI technique as the main disruption mitigation system on ITER [Jachmich22].

The database of discharges analised in this Thesis project considers the plasma evolution from the plasma current flat-top phase, where the main plasma parameters are in steady state conditions, to the thermal quench (TQ), which is a sudden drop of plasma thermal energy occurring on a time scale of the order of $1ms$, and to the current quench (CQ), which is a fast current descent with typical duration of a few tens of milliseconds.

In the following, an Ohmic plasma experiment devoted to radiation asymmetry studies is introduced to describe the chain of events just before and after the SPI activation. These chain of events are summarised in the sketch reported in Fig. 3.1 for simplicity.

Fig. 3.2 represents a typical discharge with a plasma current $I_p = 2$ MA, toroidal magnetic field $B_t = 2.25$ T, pre-disruption core electron temperature $T_e^{core} = 1.3$ keV and pre-disruption core line integrated electron density $n_e^{core} = 0.2 \times 10^{20} m^{-2}$. The time evolution of these quantities are reported in Fig.3.2 (a,b,c), respectively.

A common feature of this type of experiments is the presence of an n=1 3D magnetic field with constant phase, which is induced by the EFCC system, as described in Section 2.2. The time evolution of the n=1 EFCC current is shown in 3.2(d). The application of this external magnetic field perturbation causes a slow decrease of the line-integrated density, between $t = [15, 16.8]$s as shown in Fig. 3.2(c). This is typically called density pump out and leads to the formation of a low density locked mode [Vries11].

The time behaviour of the $n = 1$ locked mode amplitude and phase, calculated by linearly combining saddle coil measurements described in Chapter 2, is reported in Fig. 3.2(e). Note that the phase of the mode is fixed at a certain toroidal position because the mode is locked to the external magnetic field. The onset of the locked mode is detected in real time by the JET locked mode detector, which triggers the SPI when the $n = 1$ B_r amplitude is above a threshold of 10.6 mT.

As the locked mode detector raises the alarm, the SPI is activated and a frozen pellet with diameter $d = 8.1$ mm and length $l = 12.96$ mm is shot from the cold head of the injector. The SPI system allows the injection of pellets with various chemical compositions, such as pure Deuterium (D), Neon

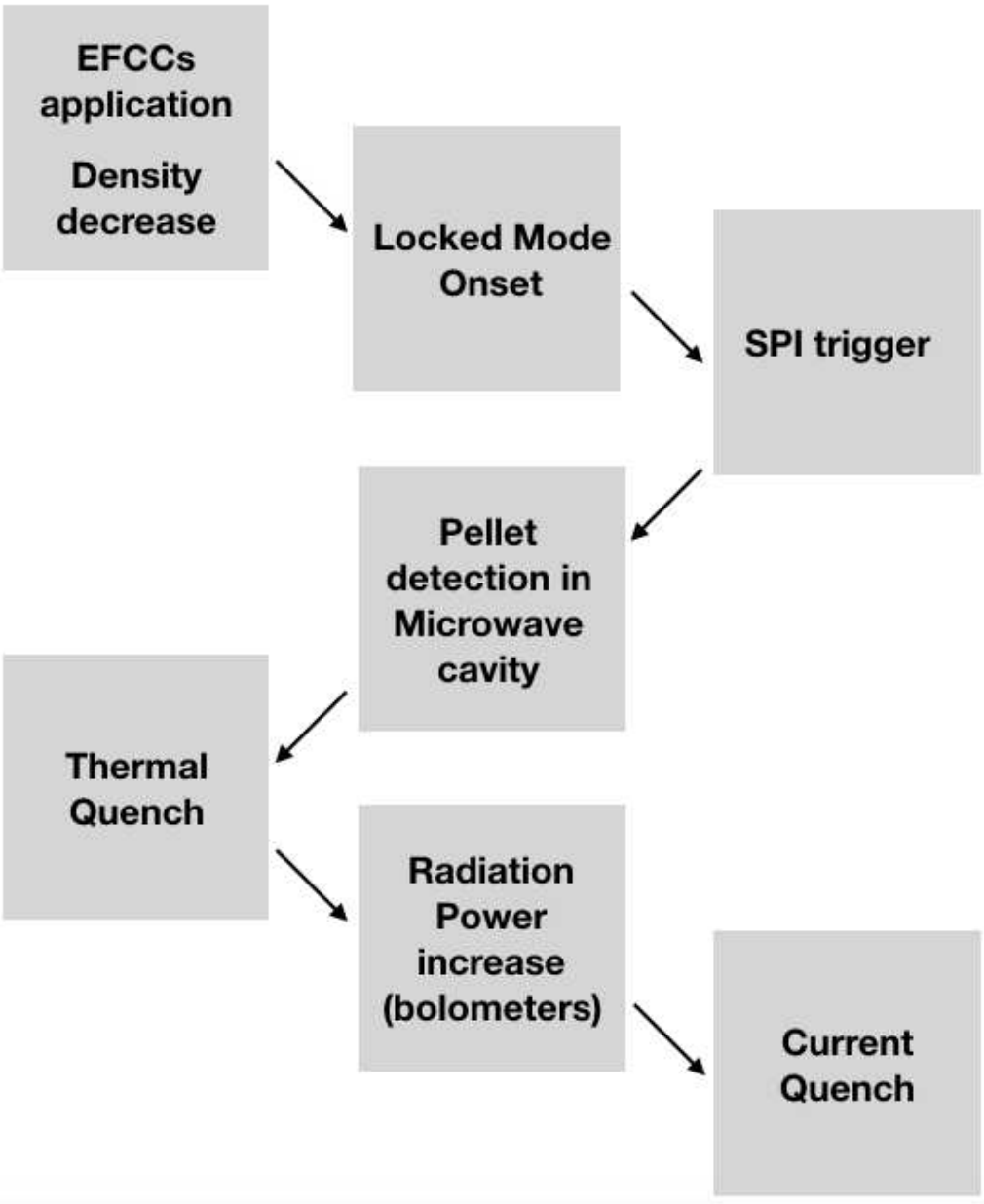

Figure 3.1: Schematic flow chart of the plasma events in radiation asymmetry experiments.

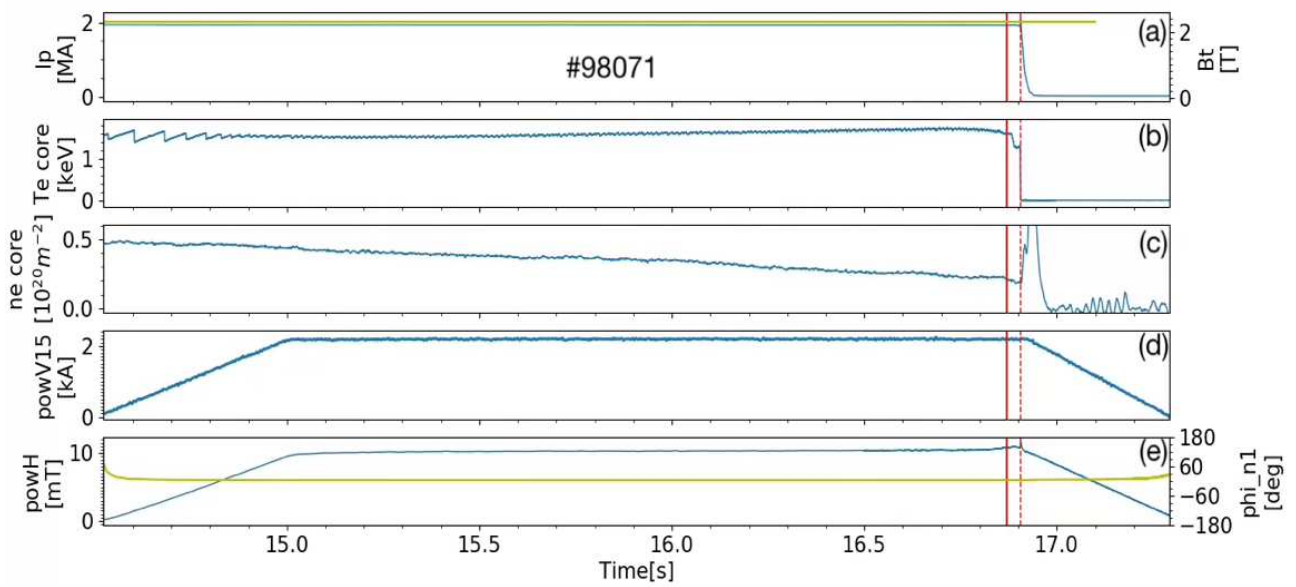

Figure 3.2: Time evolution of (a) plasma current (in blue) and toroidal field (in yellow), (b) core temperature, (c) core line integrated density, (d) EFCC current in octants 1-5 and (e) locked mode amplitude (in blue) and phase (in yellow). The vertical solid red line indicates pellet passage in microwave cavity, while the vertical dashed line indicates pellet arrival in the vessel.

(Ne), Argon (Ar) or a mixture of them. In the discharges analysed in this work, the pellet was made of a D shell and hosts a Ne core, with a Ne/D ratio of 81%.

During its journey in the flying barrel, the pellet gets scanned by the microwave cavity system, described in Chapter 2, to check its integrity. In particular, the number of detected peaks in the microwave signal indicates the number of pieces passing through the cavity. For the discharge presented here, the pellet is intact since only a single peak can be observed in Fig. 3.3. The pellet enters the vacuum vessel at around 150 m/s, initialising the Pre-TQ, which is indicated in Fig. 3.3 with a vertical red line.

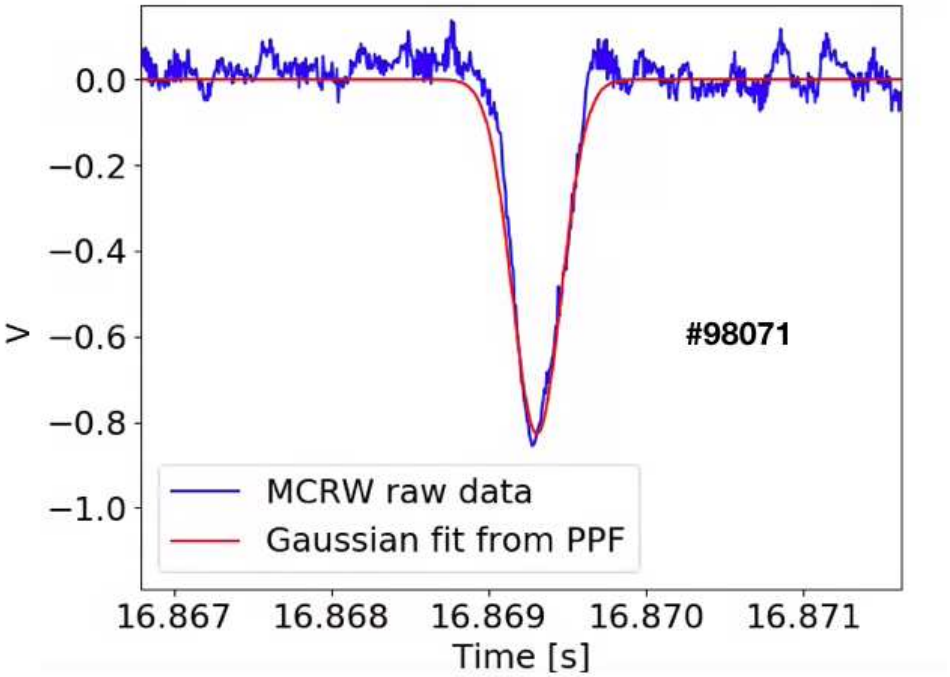

Figure 3.3: Time evolution of the microwave signal of JET #98071 pulse. The raw signal is highlighted in blue while the red line is a Gaussian fit of the peak.

Once the shattered pellet enters the vacuum vessel, a bright flash can be observed in KLB-E8WA fast camera videos as shown in the sequence of frames reported in Fig. 3.4, which covers the time period from the pellet arrival to the CQ. When the shard plume has pierced the plasma, the typical TQ behaviour (fast temperature drop) is detected by the ECE diagnostic, as shown in Fig. 3.5(b). It is worth mentioning that the plasma is cooled down from the edge to the core as the shard plume travels through the plasma column, so the thermal collapse affects the radial profile of all plasma quantities.

Since the thermal energy is strictly related to temperature, during the TQ the plasma energy must be released in some way. In unmitigated plasma disruptions, such energy is deposited onto the wall, potentially damaging the first wall structures because of the thermal and electromagnetic forces deposited. In the case sunder investigation, the plasma energy is released through radiation, which can be measured at JET by the vertical and horizontal bolometers, described in Chapter 2.

The time evolution of vertical and horizontal radiation is shown in Fig. 3.5(d-e), respectively. Both bolometric radiation measurements are taken as the total integrated power over the poloidal cross-section from all the 24 line of sights (see Fig. 2.8), assuming toroidal uniformity. Both bolometers detect a radiation peak, which is followed by a decrease while the plasma enters the CQ phase.

It can be observed that the peak of the vertical and horizontal bolometer are almost simultaneous, but a closer look reveals that the vertical signal slightly precedes the other one; this is expected since the SPI is located closer to vertical bolometer than to the horizontal one.

In this project, focus has been put on the radiation peak detected by the bolometers. Indeed, this represents the instant of stronger radiation deposition, therefore the one during eventual asymmetries have the largest effects onto the machine's walls. This time instant is defined as t_{max}, and the metrics

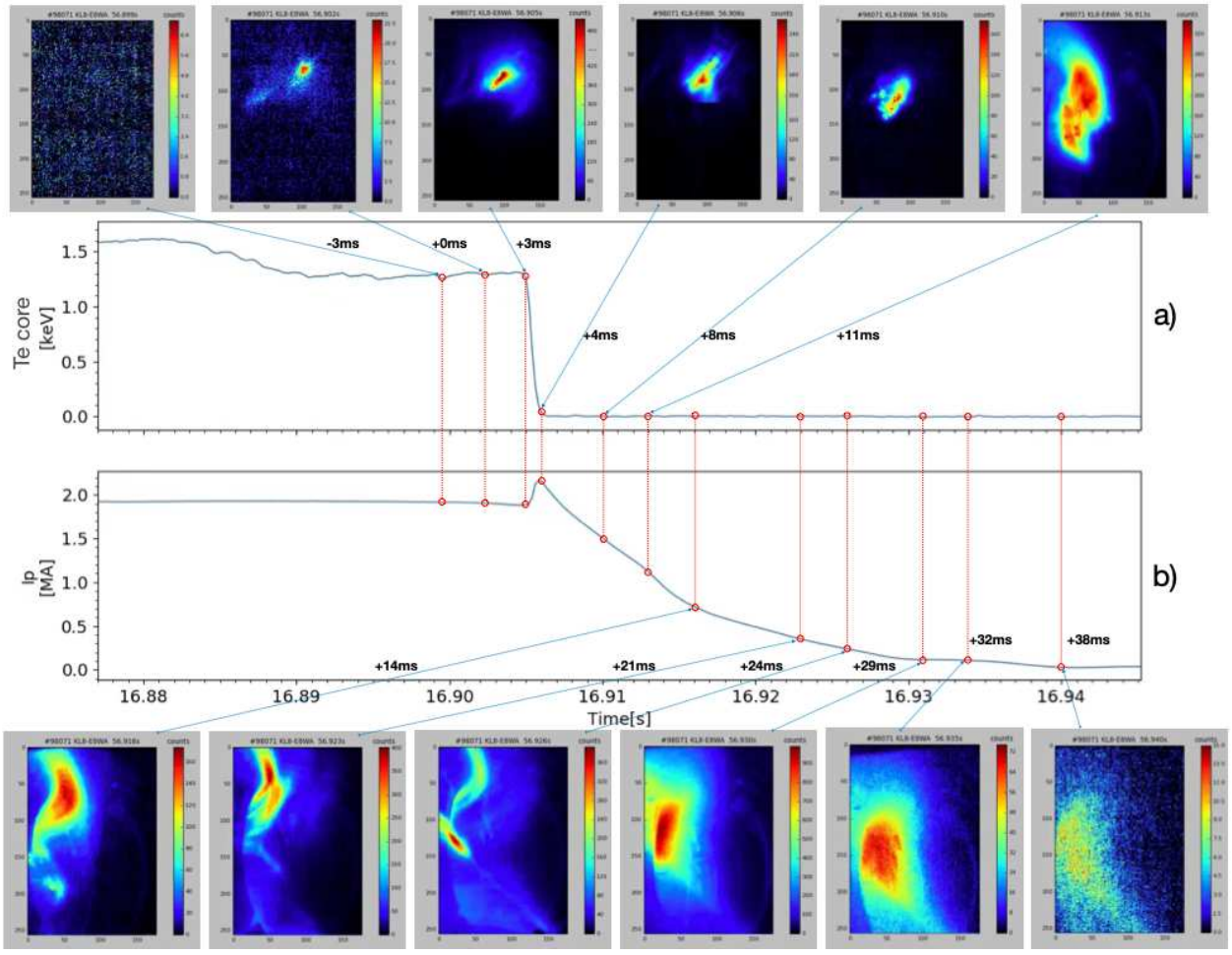

Figure 3.4: Time evolution of (a) the electron temperature and (b) the plasma current during the TQ and CQ phases. Fast camera frames during the TQ and CQ are reported as well. Data refers to JET #98071 discharge. Time references on the figure reference to the observed shard arrival from KL8 camera.

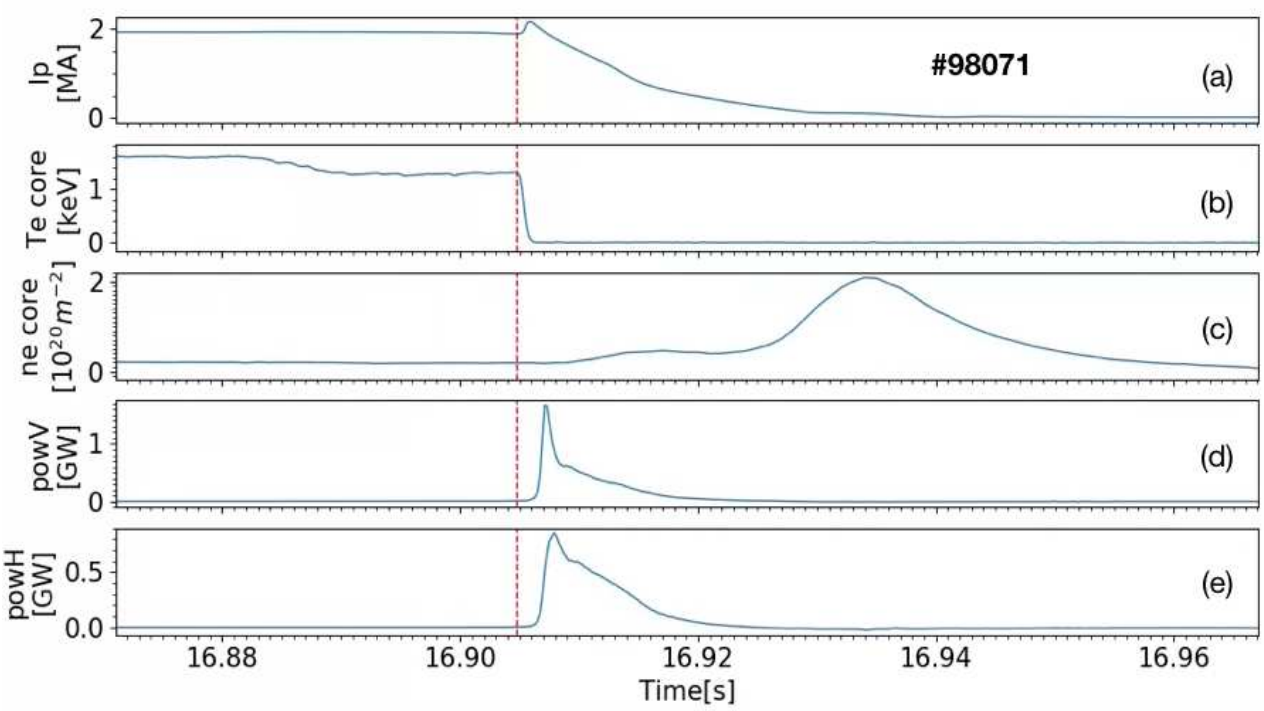

Figure 3.5: Time evolution of (a) plasma current, (b) core electron temperature and (c) line integrated density during disruption. The bottom two graphs are the detected power from (d) vertical and (e) horizontal bolometers. The vertical dashed red line indicates pellet arrival in the vessel.Note that (a)-(c) are the same of 3.2(a)-(c), but zoomed in to better show disruption dynamics.

defined in Chapter 4 are computed at this time instant. At the beginning of the CQ, as shown in Fig. 3.5, plasma current peaks as consequence of conservation of magnetic energy and drop in plasma inductance, which shortly after the plasma current starts to decay [TokW]. During this phase, as displayed in Fig. 3.5(c), the electron density increases.

It is worth noting from fast camera images, shown in Fig. 3.4, that radiation lasts until the very end of the CQ, suggesting that not only thermal energy gets emitted but magnetic energy as well. Finally the CQ dynamic ends and plasma ceases to flow in the chamber. The experiment is finished and the JET data acquisition system starts to store the data until the next pulse is initiated.

3.2 SPI experiments with a broken pellet

In the previous section, the case with an intact pellet injection has been presented. However, the pellet might break after being launched. This is a case of particular interest since if this happens, the mitigation procedure can fail. Therefore, it is of primary importance to investigate the pellet's integrity.

To detect the pellet integrity, microwave cavity data and KL8-E8WA fast camera videos have been analysed. As an example, the phenomenology observed in the JET #96231 pulse is discussed below. Fig. 3.6(a) shows the time behaviour of the microwave cavity signal. Note that this signal differs from the one reported in Fig. 3.3. Two peaks are present, suggesting the presence of a broken pellet. Being the peak proportional to the mass of the scanned piece, it can be inferred that a larger piece precedes the smaller one. This is also confirmed by the fast camera images in Fig. 3.6(b), where two distinct shard plumes can be seen at 0 ms and 12 ms (with respect to the first detected plume injection at $t = 0$ms) followed by volume filling radiation.

It is worth anticipating that a different scenario can occur: sometimes the pellet is integer while flying into the microwave cavity but appears to be broken from the fast camera videos. This occurs in the #96103 discharge, described in the next Chapter. Similar analysis based on the microwave cavity signals and fast camera videos has been carried out for all SPI experiments involved in this study, in order to eliminate possible outliers which can affect the modelling results reported in Chapter 4.

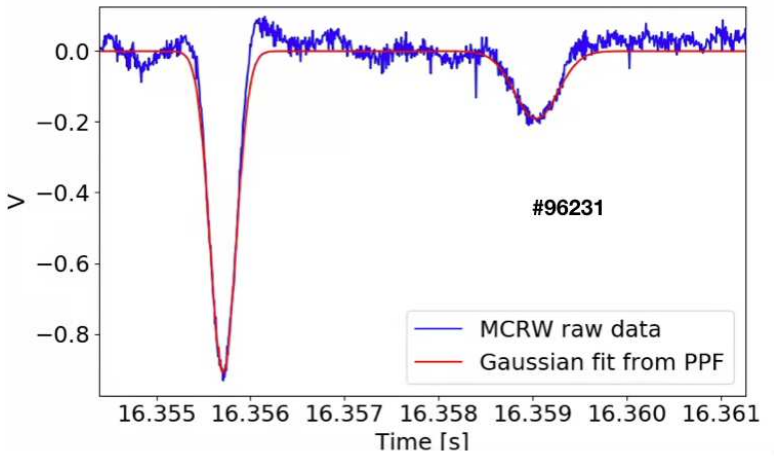

(a)

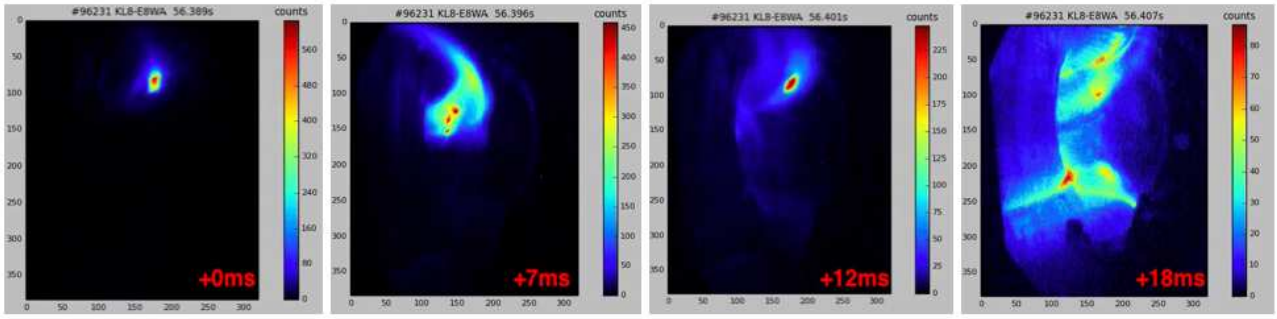

(b)

Figure 3.6: (a) Time evolution of the microwave signal of #96231 pulse. The raw signal is highlighted in blue while the red line is a Gaussian fit of the peak. (b) Left to right KL8-EW8A fast camera subsequent snapshots of the same pulse. Time references at bottom right of each snapshot refer to first detected injection.

Chapter 4

Experimental and modelling studies of radiation asymmetries

In this chapter, the theoretical model supporting radiation asymmetry studies is given, describing its origin and features. This model has been applied to the experimental results to calculate the toroidal peaking factor, which is the figure of merit used to quantify how uniformly the radiated stored energy of the plasma is spread over the toroidal surface of the plasma-facing wall.

4.1 Modelling of radiation asymmetries

The main objective of this Thesis work is the characterisation of radiation asymmetries during SPI experiments. To reach this goal, experimental data analyses have been complemented with theoretical modelling, which as will be described in this section.

4.1.1 The need for a theoretical model

The theoretical model adopted in this Thesis is the one proposed by *S. Jachmich and M. Lehnen et al.* in [Lehnen15], developed for studying radiation asymmetries with MGI in the presence of a n=1 locked mode and later adapted in [Jachmich22] to suite the SPI system.

The model has been developed to overcome the limited bolometry coverage on JET. In fact, JET can provide integrated radiation power measurements in only two toroidal positions, i.e. at $\phi_V = 90°$ for the vertical fan, P^V_{rad}, and $\phi_H = 225°$ for the horizontal fan, P^H_{rad}. Here, the positions are expressed with respect to the Octant 1, as described in Chapter 2 and shown in Fig.2.7(a). Both of these radiation measurements are taken as the total integrated power over the poloidal cross-section from the 24 line of sights, assuming toroidal radiation symmetry.

It is clear that a better coverage of the bolometry along the torus would provide a more accurate radiation detection. For example a better scenario would be having JET equipped with a couple of vertical and horizontal bolometers per octant, evenly spaced along the machine and providing local power measurements. This scenario would directly provide the power profile along the toroidal direction and asymmetry considerations would be straightforward once multiple pulses are performed. Unfortunately, this is not the case on JET and a different approach had to be found.

Jachmich's and Lehnen's model [Lehnen15],[Jachmich22] proposed a *fitting procedure*, from which the radiation power profile can be indirectly reconstructed. The basic idea behind this approach is the following: the model assumes that the radiated power $P_{rad}(\phi)$ is dependent on a set of free parameters. These parameters can be determined by fitting the so-called Radiation Asymmetry Factor (RAF), defined in 4.1, computed based on the P^V_{rad} and P^H_{rad} measurements. The radiated power distribution $P_{rad}(\phi)$ can be reconstructed, circumventing the shortage of diagnostic coverage.

4.1.2 Model description

The RAF is defined by the following expression:

$$RAF = \frac{\Delta P}{\Sigma P} = \frac{P_{rad}(\phi_V) - P_{rad}(\phi_H)}{P_{rad}(\phi_V) + P_{rad}(\phi_H)}, \tag{4.1}$$

i.e. the difference between the vertical and the horizontal measured radiation divided by their sum.

This metric does not consider radiation from the divertor region. In principle, the channels looking straight into the divertor region should give the largest contribution to the measured power, as the divertor is exactly designed to relax the excess energy flow in the machine and improve confinement quality. On the contrary, during these disruption mitigation experiments, extremely intense radiation is emitted from the bulk plasma, at least one order of magnitude greater that the divertor's contribution. For this reason, the divertor's impact is neglected in the following analysis.

In this study, another metric has been considered: the Toroidal Peaking Factor (TPF). The TPF is defined in the following way:

$$TPF(\phi_{n=1}) = \frac{max(P_{rad}(\phi_{n=1}))}{< P_{rad}(\phi_{n=1}) >} \tag{4.2}$$

It represents the maximum radiated power achievable in the presence of a $n = 1$ mode, normalised to the average radiated power. In particular $\phi_{n=1}$ corresponds to the toroidal location of the O-point of the locked mode, calculated from mid-plane saddle loops, as described in Chapter 2.

The TPF is a crucial parameter that describes toroidal asymmetry. Indeed, its toroidal distribution describes where the most powerful flash of light is deposited respect to the whole radiation present in the chamber, or in another words it represents the location where the machine is most stressed from the intrinsic radiation asymmetry. Therefore, it can be regarded as a parameter quantifying the mitigation procedure's ability to smooth out the released radiation over the toroidal angle: a large TPF means poor mitigation quality and viceversa.

The TPF alone though is not sufficient for a complete investigation of mitigation impact on plasma facing components, as it solely describes toroidal effects. Hence it is usually associated to its poloidal counterpart, the Poloidal Peaking Factor (PPF). The product of these two quantities, i.e. TPF $\times$ PPF, gives a good estimation of the overall radiation asymmetry. For example, to prevent Beryllium melting in ITER assuming a TQ of $1ms$, this product must be lower than $720MJ/E_{th}$, where E_{th} is the plasma's thermal energy at disruption time [Lehnen15]. The PPF analysis is not considered as it is beyond this thesis work.

As already mentioned, the 1D radiation model assumes that the radiated power $P_{rad}^{n=1}$ depends on the toroidal angle and is parametrically dependent on the phase of the $n = 1$ locked mode as follows:

$$P_{rad}^{n=1}(\phi) =< P_{rad}^{n=1} > n_i(\phi) p_{dis}^{n=1}(\phi) \tag{4.3}$$

where $< P_{rad}^{n=1} >$ is the radiated power averaged over the toroidal angle:

$$< P_{rad}^{n=1} >= \frac{\int_{-\pi}^{\pi} P_{rad}^{n=1}(\phi) d\phi}{\int_{-\pi}^{\pi} d\phi} = \frac{1}{2\pi} \int_{-\pi}^{\pi} P_{rad}^{n=1}(\phi) d\phi \tag{4.4}$$

while $n_i(\phi)$ and $p_{dis}(\phi)$ in 4.3 represent the injected impurity density and the impact of $n = 1$ locked modes on the power distribution. These two quantities are expressed as:

$$\begin{aligned} n_i(\phi) &= n_{i,0} \exp\Big\{ -\frac{(\phi - \phi_{inj})^2}{\lambda_\phi^2} \Big\} \\ p_{dis}^{n=1}(\phi) &= 1 + \Delta p \cos(\phi_{n=1} - \Delta\phi_{n=1} - \phi) \end{aligned} \tag{4.5}$$

where ϕ_{inj} represents the position of the SPI at 11.25°.

The amplitude of the radiated power, Δp, the width of the impurity density distribution, λ_ϕ, as well as the phase offset, $\Delta\phi_{n=1}$, are the aforementioned free-fitting parameters, while $n_{i,0}$ represents the amplitude of the Gaussian distribution of the injected impurity density. The latter quantity is not retrieved by the fitting procedure and its determination will be discussed later.

It is expected that the asymmetry is stronger when the mode is closer to the injection location, being the mode at its maximum at $\phi_{n=1}$ and being the impurity density the highest at the SPI location. Therefore, the relative position of the locked mode phase with respect to the SPI location is expected to be of primary relevance in the obtained radiation, as described in [Jachmich22] and [Lehnen15] and proved in this Thesis work.

The parameter $n_{i,0}$, as mentioned earlier, is not a free-fitting parameter. It is instead numerically computed using the fitting results and a simple analytical consideration. Let's consider the definition of the power profile $P_{rad}(\phi)$, i.e. Eq. 4.3 with a given $\phi_{n=1}$, rewriting as:

$$P_{rad}(\phi) = < P_{rad} > n_i(\phi) p_{dis}(\phi) \tag{4.6}$$

Taking the average $< ... >$ of both sides of Eq. 4.6 and substituting Eq. 4.5, one obtains

$$1 =< n_i(\phi) p_{dis}(\phi) > = n_{i,0} < \exp\Big\{-\frac{(\phi - \phi_{inj})^2}{\lambda_\phi^2}\Big\} p_{dis}(\phi) > \tag{4.7}$$

Finally, considering the average as a continuous average along the toroidal direction:

$$\begin{aligned} n_{i,0} &= \frac{1}{< \exp\Big\{-\frac{(\phi-\phi_{inj})^2}{\lambda_\phi^2}\Big\} p_{dis}(\phi) >} \\ &= \left(\frac{1}{2\pi}\int_{-\pi}^{\pi} d\phi \exp\Big\{-\frac{(\phi - \phi_{inj})^2}{\lambda_\phi^2}\Big\} p_{dis}(\phi) >\right)^{-1} \end{aligned} \tag{4.8}$$

Once the fitted parameters Δp, $\Delta\phi_{n=1}$ and λ_ϕ , are found, we can numerically compute the integral and get $n_{i,0}$.

4.2 Data analysis of radiation asymmetry experiments

The analysed database is composed of 16 Ohmic pulses performed in 2020-2021 during the so-called C39 JET campaign with a plasma current of $I_p = 2$ MA and toroidal magnetic field of $B_t = 2.25$ T. An example of these experiments is JET #98071 , which has been described in detail in the previous Chapter. A list of the discharges involved in this Thesis and the corresponding specifications of the SPI are summarised in Table 4.1.

Pulse Number	Pellet composition (no shell)	Barrel
96026	100% Neon	B
96028	100% Neon	B
96103	100% Neon	B
96231	100% Neon	B
96237	100% Neon	B
96238	100% Neon	B
98067	100% Neon	B
98069	100% Neon	B
98071	100% Neon	B
98088	100% Neon	B
98089	100% Neon	B
98090	100% Neon	B
98092	100% Neon	B
98093	100% Neon	B
98094	10% Neon - 90% Deuterium	B
98095	10% Neon - 90% Deuterium	B

Table 4.1: List of the Ohmic database analysed and the corresponding pellet settings.

In all these pulses, an n=1 magnetic field perturbation has been applied by means of EFCCs to induce a locked mode at various toroidal locations. The behaviour of radiation at different toroidal locations has been analysed in details. In particular the RAF metric has been computed according to Eq. 4.4 at $t = t_{max}$, defined as the time instant of maximum detected power from the horizontal and vertical bolometry.

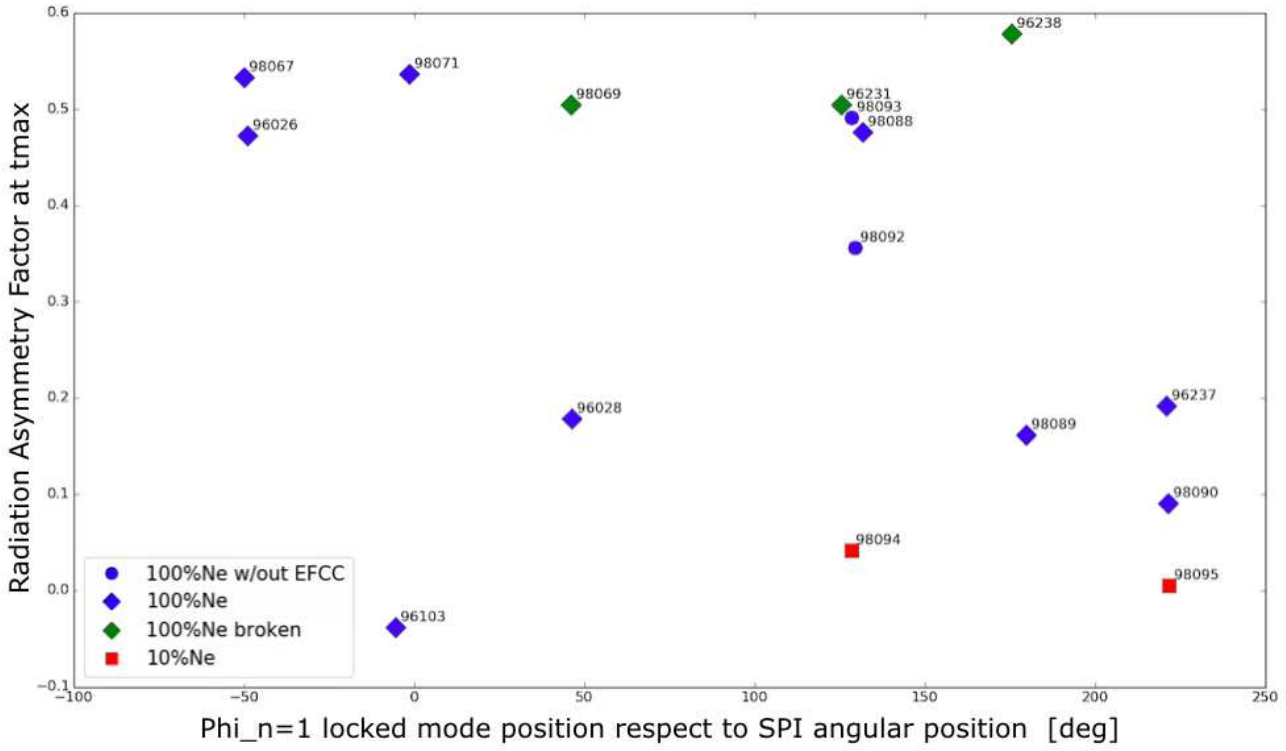

Figure 4.1: Radiation Asymmetry Factor as a function of the n=1 mode O-point phase, $\phi_{n=1}$, in the SPI frame. Data refers to the Ohmic database. Blue and green dots represent 100% Neon pellets while red squares represent 10% Neon pellets. Every datapoint is coupled with its pulse number.

Fig. 4.1 shows the RAF metric plotted against the location of the n=1 O-point phase in the SPI frame of reference. Different colours have been used to indicate pulses with various pellet compositions. In particular, the blue and the green points in the graph refer to 100% Neon pellets, red points to pellets whose composition is 10% Neon and 90% Deuterium.

A note on pellet composition has to be made: the mentioned compositions specify the relative percentage of the pellet *core*, but every pellets is covered by a Deuterium layer which should be taken into account when considering the absolute amount of impurities injected in the plasma. Hence, the 100% Neon pellet is in reality 81% Neon while the 10% Neon pellet is actually 7% Neon. The presence of the deuterium coating ensures that the pellet does not get stuck in the cold head, where it is formed, since Ne has a higher stickability to the barrel material (steel) [Gerasimov22].

Focusing on the ensemble of discharges with the 100% Neon pellet, we can see that there is a further distinction: diamonds and circles. Diamond data points indicate those pulses where EFCCs were on, while circle points were pulses without EFCCs and were considered reference pulses; reference pulses are plasma operations run without artificial mode locking. Finally, green diamonds are pulses where the microwave cavity detected more than one piece passing through it, i.e. a broken pellet. These pulses are studied here to examine if and how much the pellet breakage could affect the radiation asymmetry emission.

From Fig. 4.1 is not possible to extrapolate a clear trend, even though it can be seen that the majority of the data points closer to the SPI injection location ($\phi = 0°$) tend to have higher RAF values that those further away. This is what is expected from the model.

Furthermore, the analysis helps to identify the presence of *outliers*, i.e. unexpected RAF values which need to be investigated. First of all, the two 10% Neon cases (red squares in Fig. 4.1) are

excluded from the fitting due to their different composition , thus the RAF is expected to assume different values, as described in [Lehnen15]. Just to be clear, the 10% Neon cases are not outliers, they are just different from the 100% Neon case, as expected. Secondly, some 100% Neon pellets, such as in pulses #96103 and #96028, show a RAF value different with similar phase of the n=1 locked mode other discharges with similar phase of the n=1 locked mode. Further analysis on these pulses has been performed in order to understand their different behaviour and assess if the model needs to be corrected or not.

Pulse Number	Pellet Composition (no Shell)	Barrel
96034	100% Neon	B
96107	100% Neon	B
96109	100% Neon	B
96116	100% Neon	B
96236	100% Neon	B
96239	100% Neon	B
96794	100% Neon	B
96796	100% Neon	B
96872	100% Neon	B

Table 4.2: List of the H-mode database and the corresponding pellet settings.

Despite the fact that this Thesis project has focused on analysing radiation asymmetries in Ohmic JET plasmas, the same workflow has been applied to an H-mode database made up of 9 pulses reported in Table 4.2. This is the same database used in [Jachmich22]. In all these pulses, the pellet remained intact before shattering and was composed of 100% Neon, excluding the outer Deuterium shell.

The H-mode database differs from the Ohmic one only for the presence of auxiliary heating systems that allow the plasma to transit into the H-mode [Wagner84], and thus reaching higher thermal energy around 2 MJ, respect the Ohmic scenario, which usually has thermal energy below 1 MJ.

In the H-mode scenario typically 10 MW of Neutral Beam Injection (NBI) power and 2 MW of Ion Cyclotron Resonance Heating (ICRH) are applied. Similar to the Ohmic scenario, n=1 magnetic field perturbations are applied by means of EFCCs. The RAF values as a function of the locked mode phase with respect to the SPI position for the H-mode database are shown in Fig. 4.5(a).

Radiation asymmetry studies have been performed in the H-mode regime to assess the possible role of the plasma store energy on the TPF. A detail comparison among these databases is beyond the scope of this work. Further analyses are planned in the near future considering new experiments, which will be performed at JET in April 2023.

4.2.1 Investigation of outlier pulses

In this section, the so-called *outlier* pulses in the Ohmic database are examined. These are the pulses whose RAF value was unexpected or very different from all other neighbouring points.

For presentation purposes we only report the comparison between #96103 and #98071 discharges, only. The comparison has been performed considering the behaviour of the TQ, the CQ and bolometric power detection during the mitigation process. This information is integrated with fast camera images, to deeply understand the dynamic of the pellet when entering the plasma.

#96103 vs #98071

The considered outlier is pulse #96103, whose RAF is much lower than the nearby data. As shown in Fig 4.1, this pulse is found to have a negative RAF. Such case, even though being not in line with all other discharges, is not excluded by the definition of RAF in Eq. 4.1: if the maximum of the horizontal power happens to be larger than the the maximum of vertical one, then RAF is negative. What is truly unexpected though is that the absolute value of #96103 is about 10% of the value of the reference pulse (#98071), even though the two data points are approximately at the same toroidal

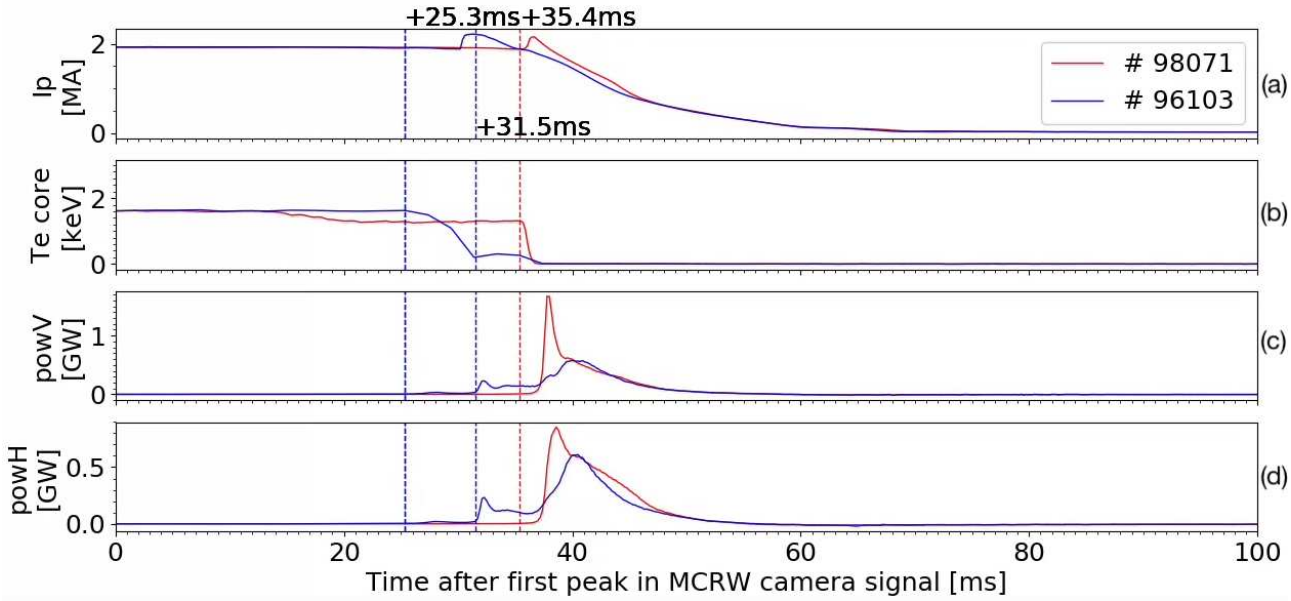

Figure 4.2: Comparison between #98071 (good) and #96103 (outlier). Time behaviour of (a) plasma current, (b) core electronic temperature, (c-d) vertical and horizontal time traces. Dotted vertical lines indicate the pellet time of arrival in the vacuum vessel taken from fast camera videos, while time traces refer to the time instant of microwave signal peak.

location. Such a low value happens only if the numerator of Eq. 4.1 is very close to zero, hence $P_V \approx P_H$ at t_{max}.

Fig 4.2 shows the time evolution of plasma current, core electron temperature, vertical and horizontal detected power of #96103 discharge (blue) and #98071 discharge (red). The dotted lines in the figure indicate the shard arrival in the plasma, as deduced from fast camera analysis.

From a first glance, it is clear that both the TQ and the CQ dynamics in #96103 differ from those in #98071. In #96103, as shown in Fig. 4.2(b), it is possible to recognise two phases during the TQ: the first characterised by a slow temperature decrease, while the second shows a constant temperature plateau. On the other hand, in #98071, the TQ corresponds to a more drastic temperature drop. Moreover, as shown in 4.2(a), in #96103, the CQ phase is much longer with respect to the #98071 one.

This peculiar behaviour is due to the broken pellet entering in the plasma, as demonstrated by bolometry. As shown in Fig. 4.2(c-d), two peaks can be detected in the time evolution of the vertical and horizontal radiation signals, respectively. This indicated that some radiation, arguably from the injected impurities, is detected at two stages, suggesting two separate impurity assimilation processes.

Although the microwave cavity signal in Fig.4.3(a) shows a single peak, hence an intact pellet flying through it, fast camera images in Fig. 4.3(b) proves the hypothesis of pellet breakage after the microwave cavity. Indeed, from Fig. 4.3(b), multiple pellet injections are detected at -7 ms and 0 ms, where time instants reference to the injection that triggered the first disruption effects (first slow temperature drop in 4.2(b)), are observed before the main injection at +6 ms. Henceforth it is clear that more than one piece were injected at different time instants in #96103.

Based on these experimental evidences, it is possible to conclude that the disruption dynamics is different in these two pulses because of the unexpected multiple pellet injection. The pellet could have broken due to internal weak points arising from the freezing process; being not sturdy enough, during its travel in the flying barrel collisions with the barrel structure made the pellet fracture. It can be argued that if the larger pellet chunk had arrived earlier than the smaller piece, the dynamics could have been more similar to the standard experimental trend.

The analysis of the TQ and CQ, the plasma radiation, the microwave cavity and the fast camera signals has been carried out for all the database of discharges to discriminate pulses with intact/broken pellet. For the fitting purposes, every pulse with a broken pellet was removed from the dataset. For reference, we reported in Table 4.3 the Ohmic discharges that have not been included in the fitting procedure and the corresponding motivation. The same approach has been taken by the authors of

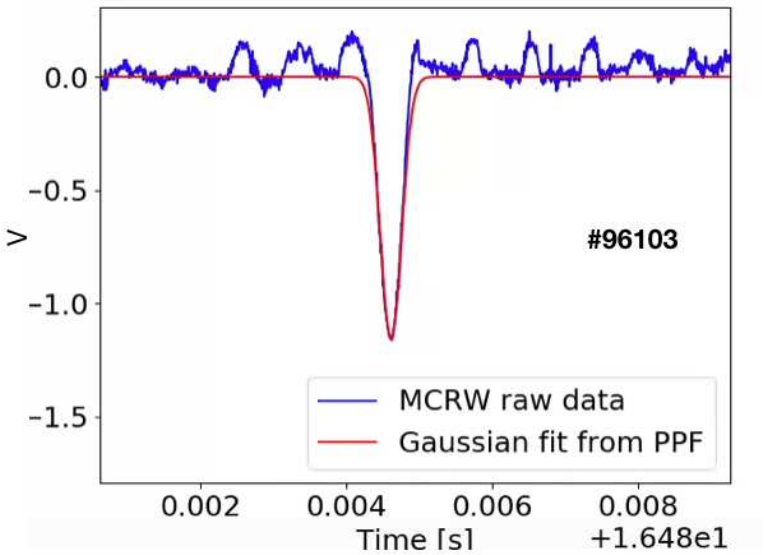

(a)

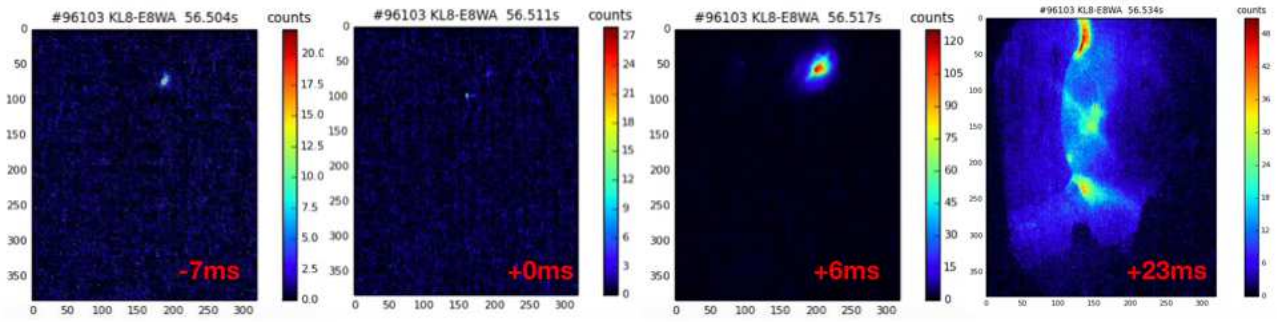

(b)

Figure 4.3: (a) Microwave signal for #96103 pulse. One are detected, suggesting the pellet is integer when scanned. (b) KL8-EW8A fast camera subsequent (left to right) snapshots of pulse #96103. Time reference to the material injection that triggered the first disruption effects (first slow temperature drop in 4.2(b)).

Pulse n°	Rejection reason
96028	Broken
96028	Broken
96103	Broken
96238	Broken
98069	Broken
98092	No EFCCs
98093	No EFCCs
98094	10% Neon
98095	10% Neon

Table 4.3: Table summarising the reason why some of ohmic pulses have been excluded from the fitting analysis. No EFCCs pulses are reference pulses where no current was driven in Error field correction coils.

[Jachmich22] when analysing the H-mode database.

4.2.2 RAF Fitting and TPF Results

After filtering out the outliers in the Ohmic database using the method discussed in the previous section, one can proceed with fitting the toroidal distribution of the RAF and using the fit results to calculate the TPF. To reach this goal, a procedure has been implemented in the Python framework [GitHub]. In particular, the routine used to fit the experimental data is the Python *curve_fit* routine, which uses non-linear least squares to fit the data and is part of the *SciPy.optimize* package.

Since every shot is unique and it has not be possible to assign a statistical error to the RAF value, error bars are evaluated by the sensitivity error of the bolometers, which is 10% of the measured value. Consequently, the propagated error associated to each RAF data point is 20% of the value itself. The experimental RAF values, together with the assigned errors, are shown in Fig. 4.4(a) as a function of the relative position of the locked mode O-point $\phi_{n=1}$ respect to the SPI injection location ϕ_{inj}. Considering instead the error associated to the locked mode position, this should be computed from the saddle loop error of 1.5% respect to the measured *flux*; although one should consider the specifics of how the saddle loops signal are combined to give the locked mode position, and then propagate the errors accordingly, a simpler approach was followed due to the relative interest in the error associated to this quantity. Instead, the 1.5% was associated to the already combined saddle loop signal for the *sine and cosine* of the locked mode perturbation, whose position is given by $\phi_{n=1} = \arctan(\sin(\phi_{n=1})/\cos(\phi_{n=1}))$. Propagated errors are of the order of $\approx 1°$. Looking to Fig. 4.4(a), it can be observed that a couple of points around 135° are further one to another more than 1°, suggesting if the simple estimation given to the errors in incorrect: this is actually not the case since it has been discovered that currents in EFCCs for that couple of pulses, which should be the same, are slightly different. It is thus believed that it is such current discrepancy which gives different locked mode positions.

The *curve_fit* routine has been applied to the experimental RAF points. The input fitting function is the RAF definition reported in Eq. 4.1, while free-fitting parameters are the output of the *curve_fit* routine as solution to the non-linear least squares problem set by the function. The results of such fitting procedure are shown in Fig. 4.4(a) with a dashed blue line for the RAF. Note that in the figure a orange band is also present. This band represents all the possible resulting fitting curves due to the presence of errors computed from the covariance matrix. Results and associated errors are reported in table 4.4.

The numerical results for the ohmic fit, i.e. $\Delta p = 0.36$, $\Delta\phi_{n_1} = -24°$, $\lambda_\phi = 127°$, are summarised in table 4.4. The associated error to each fitting parameter , shown in the table, is computed using the standard deviation computed from the covariance matrix, output of the fitting routine.

These fitting parameters, as mentioned before, have been used to compute the TPF, defined in Eq. 4.2. In particular, the numerator of Eq. 4.2, i.e. the maximum value of $P_{rad}(\phi_{n=1})$, is the maximum value of the power distribution P_{rad} along a complete toroidal turn for a given locked mode position

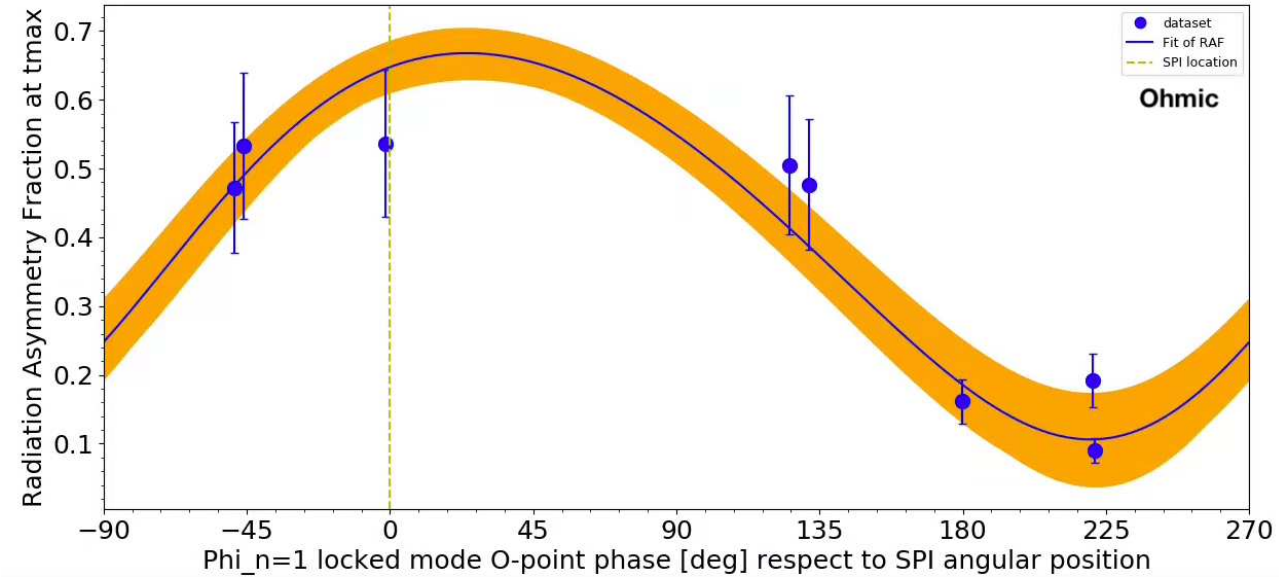

(a)

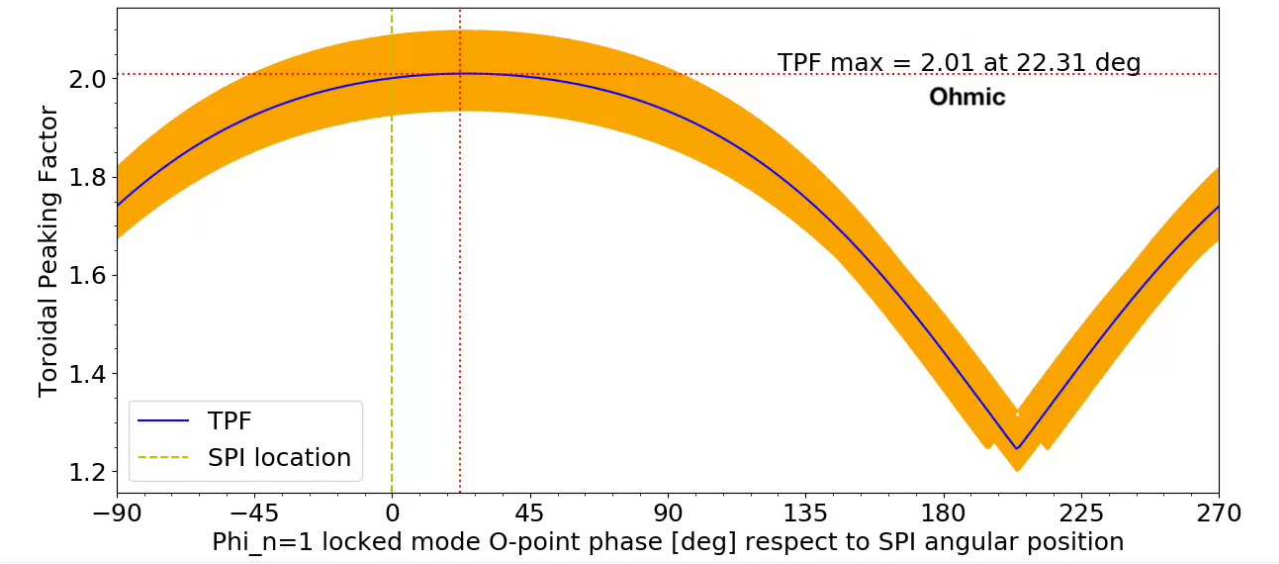

(b)

Figure 4.4: (a) RAF calculated at t_{max} as a function of the relative position between the locked mode phase $\phi_{n=1}$ and the SPI location ϕ_{inj} for the Ohmic dataset. The solid blue line represents the resulting fitting curve, while the orange band represents the the range defined by the errors from RAF statistical analysis, see table 4.4. (b) The TPF curve as a function of the relative position between the locked mode phase $\phi_{n=1}$ and the SPI location ϕ_{inj} resulting from the fitting parameters. The orange band comes from computing the TPF from the free fitting parameters where errors were considered. The SPI position is highlighted by a yellow dashed line.

Scenario	Δp	$\Delta\phi_{n=1}$	λ_ϕ	Max TPF
Ohmic	0.36 ± 0.06	$-24° \pm 10°$	$127° \pm 9°$	2.01 ± 0.08
H-mode	0.18 ± 0.02	$-8° \pm 6°$	$166° \pm 5°$	1.59 ± 0.04

Table 4.4: Result of the fitting procedure applied to the Ohmic database and the H-mode database, together with the associated errors. Maximum value for TPF and associated error is reported as well.

$\phi_{n=1}$. The denominator is instead computed as a continuous average along the toroidal angle ϕ for each locked mode position. Finally, to include a toroidal dependence on P_{rad}, the same procedure has been repeated $N = 360$ times. The number N is arbitrary and it does not affect the accuracy of the computation. The value chosen ensures the resulting curve is not pointy.

The calculated TPF of the Ohmic database along the $\phi_{n=1}$ O-point location respect to the SPI location is reported in Fig. 4.4(b). Note that the TPF has a maximum value of 2.01 at $\phi_{max} = 22.3°$. The corresponding ΔTPF is the deviation from the TPF value and the TPF computed from the fitting parameters comprising of their errors, i.e. RAF $\pm\Delta$RAF was given as input.

As mentioned before, the workflow described above has also been applied to a set of H-mode plasmas devoted to radiation asymmetry studies, described in [Jachmich22]. The corresponding results are reported in Fig. 4.5, while the free-fitting parameters obtained by applying the *curve_fit* routine to the toroidal distribution of the RAF function are included in Table 4.4

Comparing the free-fitting parameters reported in Table 4.4, it is clear that radiation asymmetry in Ohmic and H-mode plasmas behaves differently. In particular, a larger TPF value has been obtained analysing the Ohmic plasmas. This implies that in H-mode the radiated energy tends to be spread more symmetrically along the toroidal angle. The first obvious finding from this database is that disruptions with high stored energy have a considerably lower radiation asymmetry compared to those with less energy. This results is consistent with that reported in [Lehnen15] for MGI instead of SPI.

In [Lehnen15], RAF analysis shows that pulses with diamagnetic energy E_{dia} greater than 3.5 MJ have a much lower RAF free parameter values, suggesting a better symmetry in the mitigation. Moreover RAF is plotted against E_{dia} for various shots and it is clear that it diminishes as diamagnetic energy grows.

Henceforth considering the results found in [Lehnen15] and in this Thesis, it is legit affirm the impact of the n = 1 mode is much weaker for high energies. In the frame of this Thesis work, this different behaviour might be due to a couple of effects: the locked mode dynamics and the pellet ablation, which depends on plasma temperature, and generally speaking on the plasma scenario.

Finally to further investigate this point, 4 experimental sessions will be performed at JET in spring 2023. In particular, to assess the dependence of radiation asymmetries on the plasma thermal energy, the plasma scenario will be improved to accommodate the injection of 20 MW of NBI power, which will allow reaching plasma stored energy above 2 MJ. To better diagnose the thermal content of the plasma in preparation to this experiment, the HRTS system has been improved including 4 new spectrometers which allow to acquire low electron temperature data from the plasma edge, and in particular at the q=2 surface, where the locked mode is located.

4.2.3 Dependence of TPF from the fitting parameters

As assessed in previous MGI studies and confirmed by the analyses carried out in this project, H-mode plasmas give a lower maximum TPF value. For ITER and next step fusion reactors, such lower value is desired. It is thus straightforward to question how the TPF is correlated with the RAF fitting parameters.

To investigate this point, an academic exercise has been carried out and reported here. Considering the dependence on the phase shift $\Delta\phi_{n=1}$ as null, the maximal TPF map as function of λ_ϕ and Δp has been generated and reported in Fig. 4.6(a). In this figure, the maximal TPF value is represented. The optimal maximal TPF values are located in the top left corner of the contour plot, therefore associated with large impurity spreads and low power deviation.

Fig 4.6(b) shows the reconstructed radiated power profile from Eq. 4.6(b) for the H-mode and Ohmic dataset, as well as for two imaginary situations: an ideal scenario (TPF max = 1.47) and a non-ideal scenario (TPF max = 2.45).

Indeed, trying to reconstruct the power profile P_{rad} for such scenarios, it results flatter and more evenly spread respect to profiles related to a couple $(\Delta\phi_{n=1}, \lambda_\phi)$, resulting in higher TPF values. Seen that power is more distributed along the whole toroidal angle, radiation results more symmetrical, hence giving a lower maximum TPF as suggested from intuition.

Therefore the mentioned parameters give another tool to better understand radiation asymmetry physics and possible engineering for better performances. Based on this analysis, it is suggested to engineer pellet injection in a way to make the power profile as flat as possible, for example by modifying the SPI injection scheme for a given plasma thermal energy. This task could be tackled through simulations scenarios using the modelling code JOREK. This kind of analysis is expected to be performed as continuation of this Thesis work.

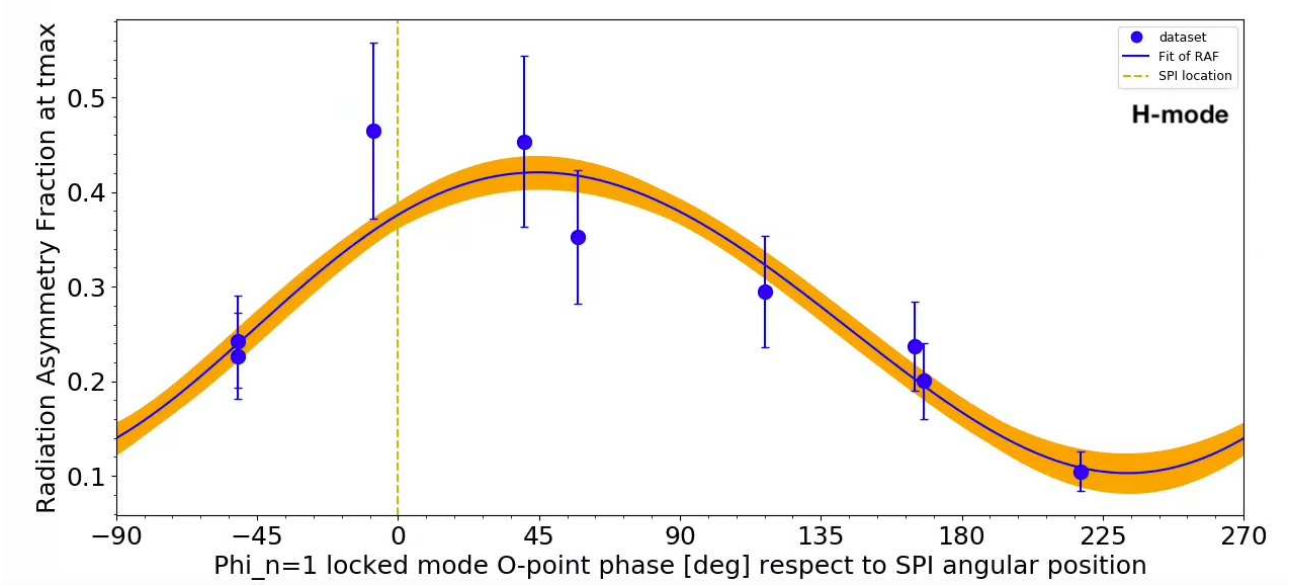

(a)

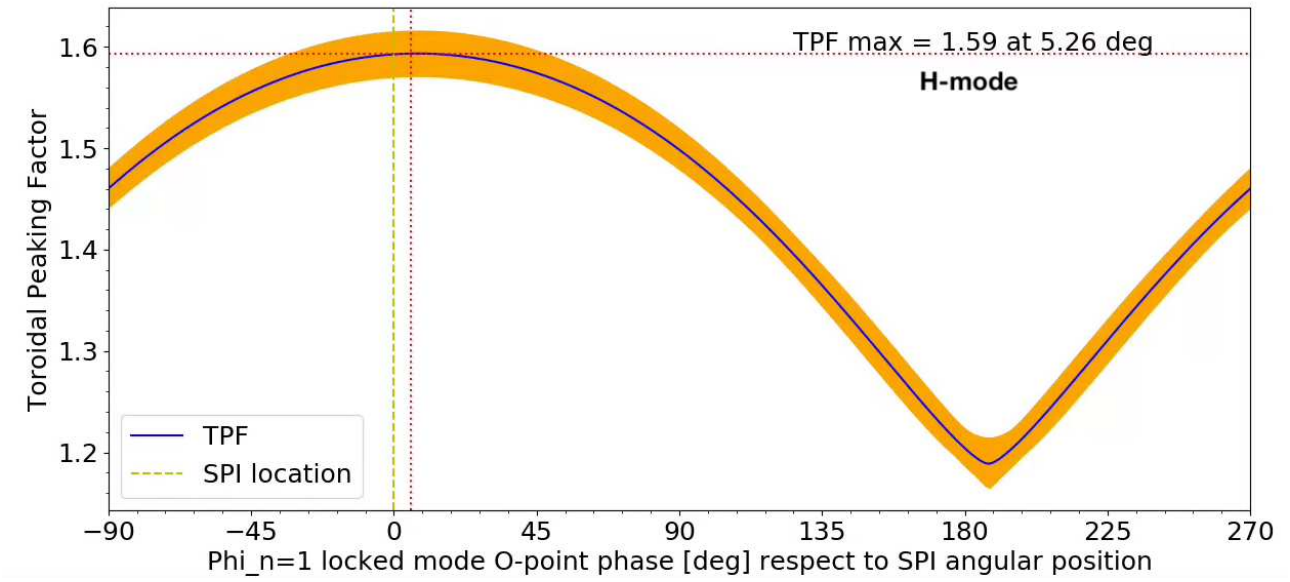

(b)

Figure 4.5: (a) RAF calculated at t_{max} as a function of the relative position between Locked mode phase $\phi_{n=1}$ and SPI location ϕ_{inj} for the H-mode dataset.The solid blue line represents the resulting fitting curve, while the orange band represents the the range defined by the errors from RAF statistical analysis, see table 4.4. (b) The TPF curve as a function of the relative position between the locked mode phase $\phi_{n=1}$ and the SPI location ϕ_{inj} resulting from the fitting parameters. The orange band comes from computing the TPF from the free fitting parameters where errors were considered. The SPI position is highlighted by a yellow dashed line..

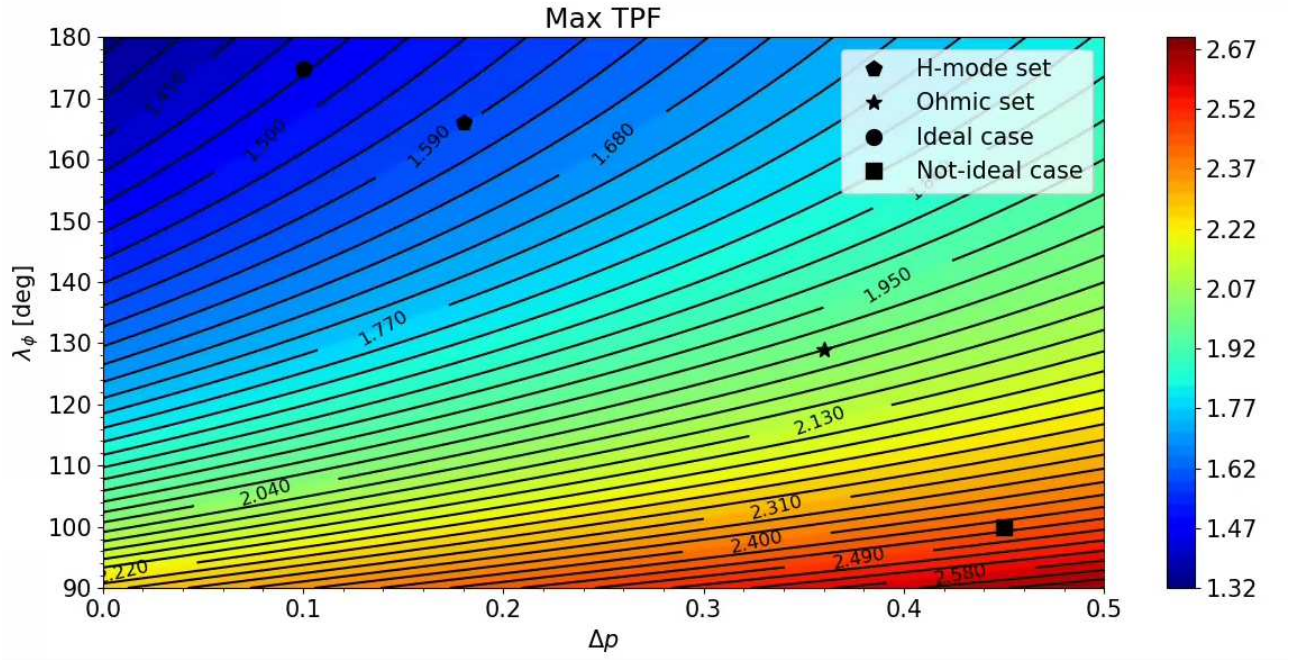

(a)

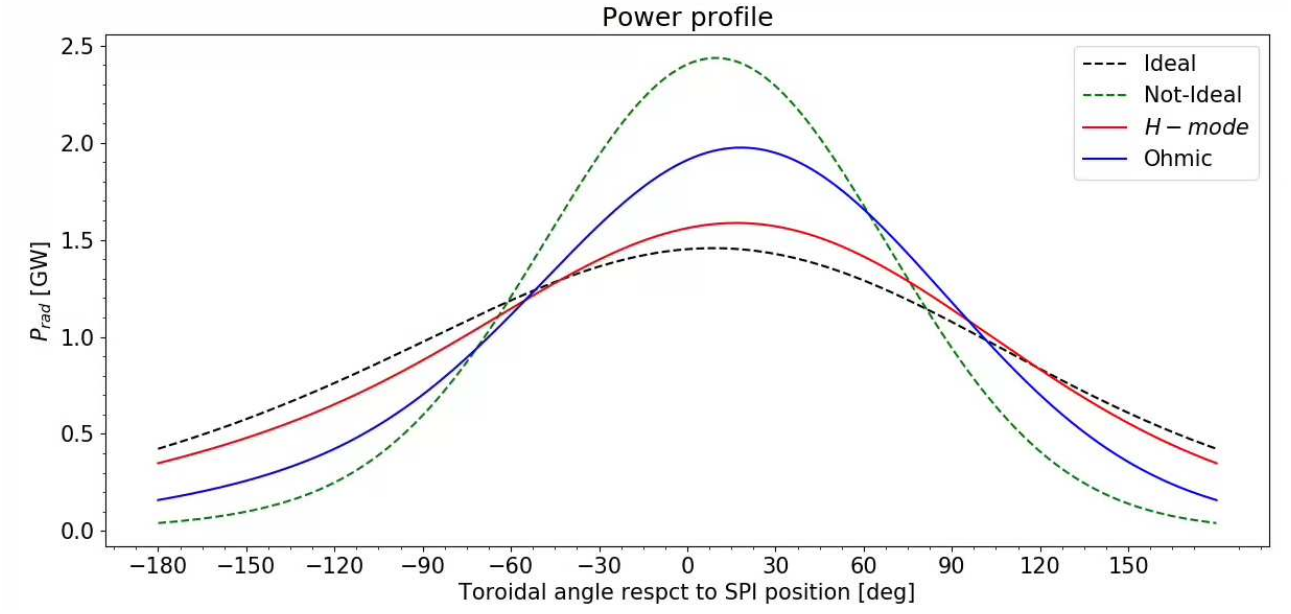

(b)

Figure 4.6: (a) 2D map showing the Maximum TPF value achievable for a given couple of $(\Delta p, \lambda_\phi)$ fit values, where black lines indicate constant TPF. Black symbols indicate the value of TPF for a particular set of scenarios: H-mode and Ohmic analysed sets and two examples, ideal and not-ideal. The interval between two adjacent black lines is 0.03. (b) Power profile reconstruction for the cases shown in (a) for a Locked mode position of $\phi_{n=1} = 30°$. Ideal and non-Ideal scenario have $\Delta\phi_{n=1} = 0°$ for semplicity.

Chapter 5

Conclusions

In magnetic fusion devices, plasma disruptions are very dangerous events, since its causes large thermal and electromagnetic loads onto the vessel walls [Hender07]. Among the various disruption mitigation techniques, the one which shows to be more effective in mitigating the effects of a disruption is the Shattered Pellet Injection (SPI). The SPI technique is based on the injection of fast impurities in the plasma to enhance radiation as energy relaxation method [Jachmich22].

Radiation asymmetries during disruption mitigation is a matter of concern, especially towards ITER. Indeed, radiation asymmetries could cause local heat loads that exceed the melting limit of beryllium of the ITER first walls [Lehnen15], [Jachmich22]. Such radiation load can be quantified through the Toroidal Peaking Factor (TPF), which represents the power radiated peak value along the torus normalised to the radiation present in the vessel during a disruption.

To investigate radiation asymmetries in a ITER-like wall machine, the SPI system has been installed at the JET device, located at Culham, UK, and a dedicated experimental campaign has been carried out.

Radiation asymmetry during mitigation via SPI has been investigated in this Thesis Project by i) analysing a database of Ohmic JET discharges performed in 2020-2021, considering data from multiple diagnostics as saddle loops, bolometer, interferometer, electron cyclotron emission, microwave cavity, fast cameras, and ii) applying a 1D radiation model for TPF data interpretation [GitHub].

Such a study has been faced by developing a series of Python routines for data analysis and modelling development. Thanks to the flexibility of the established framework, the radiation asymmetric study has been also applied in the last weeks of this Thesis project to another database of JET experiments, which are in H-mode [Wagner84], and with higher plasma energy content.

Since the bolometer coverage at JET is insufficient to determine the TPF metric, in the Ohmic and H-mode discharges analysed n=1 3D magnetic fields with various phases have been induced by means of Error Field Correction Coils (EFCCs), allowing the tailoring of the n=1 O-point phase. The dynamics of the mitigation process has been compared among the discharges, scrutinising the composition of the pellets and its integrity, which affect the radiation distribution.

For a database of similar SPI discharges, the Radiation Asymmetry Factor (RAF), which describes the asymmetry of power detection in JET's bolometers, has been calculated for different toroidal positions. The result of a fitting procedure on RAF gives a set of free fitting parameters the model's assumption of the radiated power distribution is based on. Reconstructing the radiated power, it was possible to retrieve the TPF for the considered scenario.

In both the Ohmic and the H-mode plasmas, the TPF is found to depend on the toroidal phase of the n=1 locked mode, reaching a maximum of value when the O-point position of the mode is approximately aligned with the injection. This suggests that the asymmetric heat flux due to the n=1 mode also plays a role in driving the radiation asymmetry, in addition to the localised impurity injection, i.e. SPI position.

Although sharing similar qualitative results, the TPF values differ from Ohmic to H-mode scenario. Ohmic plasmas have a maximum TPF value around 2, while the H-mode plasmas of the order of 1.6. This means that Ohmic plasmas result in a more asymmetric mitigation event, characterised by a more localised toroidal power profile, opposed to the H-mode. Therefore H-mode represents a less

threatening case for ITER.

To further consolidate this results, radiation asymmetry studies are scheduled at JET for April 2023. In these experiments, the plasma scenario will be optimised by increasing auxiliary heating power to reach higher thermal content, and thus allowing predictions on the TPF value for ITER case.

Modelling studies by JOREK code [Huysmans07] are also envisaged to complement this work. In particular, JOREK modelling will be used to check the 1D radiation model validity comparing the predicted maximum radiation load location and intensity with diagnostic data and to study the effect of an n=1 locked mode, with various amplitudes, on the mitigation process.

Although being SPI system the best solution at present for disruption mitigation in ITER, it is worth reporting that the SPI system has some down sides as well. First, there is the inconvenience of reaching ultra low temperatures to freeze Deuterium into pellets, and working in Helium Cryogenics can always be delicate. Second, it has been observed that, if for any reason the pellet breaks into two or more pieces in the pipe before getting shattered, the mitigation process can partially fail and lead to higher asymmetries. It is thus of paramount importance to carefully optimise the design of the injector to prevent this happening, for example considering multiple shattered pellet injectors.

In conclusion, being the SPI a very recent mitigation system, there are still many open questions to be answered about the physics of the mitigation. Therefore, dedicated experiments are running in several machines, as in KSTAR (Daejeon, South Korea), even considering SPI with a different geometry, to make it a robust and reliable tool for ITER machine protection.

Bibliography

[Jachmich22] S. Jachmich et al 2022 Nucl. Fusion 62 026012 (Shattered pellet injection experiments at JET in support of the ITER disruption mitigation system design)

[Lehnen15] M. Lehnen et al 2015 Nucl. Fusion 55 123027 (Radiation asymmetries during the thermal quench of massive gas injection disruptions in JET)

[Lehnen13] M. Lehnen et al 2013 Nucl. Fusion 53 093007 (Impact and mitigation of disruptions with the ITER- like wall in JET)

[Commaux16] N. Commaux et al 2016 Nucl. Fusion 56 046007 (First demonstration of rapid shutdown using neon shattered pellet injection for thermal quench mitigation on DIII-D)

[Vries11] P.C. de Vries, et al., Nucl. Fusion 51 2011 053018 (Survey of disruption causes at JET)

[Gerasimov22] S.N. Gerasimov et al 2022 Nucl. Fusion (Mitigation of disruption electro-magnetic load with SPI on JET-ILW)

[Wagner84] F. Wagner et al., Phys. Rev. Lett. 53, 1453 (Development of an Edge Transport Barrier at the H-Mode Transition of ASDEX)

[Strait15] Phys. Plasmas 22, 021803 (2015), (Magnetic control of magnetohydrodynamic instabilities in tokamaks)

[Callen11] J.D. Callen 2011 Nucl. Fusion 51 094026 (Effects of 3D magnetic perturbations on toroidal plasmas)

[Hender07] T. Hender et al 2007 Nucl. Fusion 47 S128–S202, (MHD stability, operational limits and disruptions)

[Huysmans07] G.T.A. Huysmans and O. Czarny 2007 Nucl. Fusion 47 659 (MHD stability in X-point geometry: simulation of ELMs)

[Gambrioli22] Matteo Gambrioli, Investigation of intrinsic error fields in MAST-U device, Master Thesis

[ITER-blanket] ITER website, Blanket section. link: https://www.iter.org/mach/blanket

[TokW] Tokamaks, J. Wesson, Third edition

[FP] Fusion Physics, M. Kikuchi, K. Lackner, Minh Qunag Tran

[GitHub] Analysis code repository on GitHub at https://github.com/tancready-lpp/asymmetry-SPI.git

Acknoledgements

Mi perdonerete, ma i ringraziamenti li faccio in Italiano.

Non posso che iniziare ringraziando infinitamente Lidia, la quale mi ha seguito passo passo per tutta la durata della tesi e mi ha permesso di vivere un'esperienza unica quale quella di studiare al JET. Non solo l'esperienza accademica in un importante centro di ricerca è di inestimabile valore, ma anche l'opportunità di immergersi in un mondo molto diverso da quello a cui sono abitutato. Vivere ad Oxford sarà qualcosa che mi porterò sempre nel cuore, nonostante le difficoltà che ho dovuto affrontare. Non sono solo grato a Lidia per l'esperienza che mi ha permesso di vivere, ma soprattutto per il supporto costante che mi ha dato, una settimana dopo l'altra, un meeting dopo l'altro, un messaggio su Slack la Domenica sera dopo l'altro. Grazie davvero Lidia.

Sarebbe illegale non ringraziare la mia famiglia ed in particolare mia Mamma e mio Babbo (e Marchino, non mi dimentico stavolta); non che lo faccia perchè è dovuto, bensì perché senza il loro costante supporto io sicuramente non mi troverei a scrivere questi ringraziamenti. Sinceramente non credo che potrò capire lo sforzo che hanno fatto e le preoccupazioni che gli ho procurato finchè non mi troverò nella loro situazione. Di tutto ciò che mi hanno dato però, l'amore è l'unica cosa che riesce a mettermi le lacrime agli occhi. Io non so se questo è quello che di solito si scrive in dei ringraziamenti, ma adesso che li scrivo non mi interessa. Se posso incidere con l'inchiostro una granello di quello che provo per voi lo faccio in questo momento una volta per tutte. Se solo riuscissi a fare la metà di tutto ciò che avete fatto per me in questi anni di magistrale per i miei figli, o comunque alle persone a cui voglio bene, mi sentirei realizzato. Non vorrei che Ila e Gary si sentissero esclusi, ma questo paragrafo è anche per voi. Senza la Cugina a Brighton (Worthing fa meno scena, diciamolo)

Chiaramente un grande abbraccio va a tutti i miei amici, Padovani e Fiorentini, e a chiunque abbia incontrato lungo la strada. Tanto mi conoscete, i veri ringraziamenti saranno di persona.

Last but not least, I want thank Mengdi and all my UK friends and "colleagues". She has truly been my reference point while at Culham and I'm very happy to have had the opportunity to collaborate with you. I hope we can work together again in the future and share a couple more pints.